Matrix Biology 135 (2025) 70–86

Contents lists available at ScienceDirect

Matrix Biology

journal homepage: www.elsevier.com/locate/matbio

A CNA-35-based high-throughput fibrosis assay reveals ORAI1 as a regulator of collagen release from pancreatic stellate cells

Rieke Schleinhege [a], Ilka Neumann [a], Andrea Oeckinghaus [b], Albrecht Schwab [a], Zoltán Pethő [a,*]

[a] Institute of Physiology II, University of Münster, Robert-Koch Str. 27B, 48149, Germany
[b] Institute of Molecular Tumor Biology, University of Münster, 48149, Germany

ARTICLE INFO

Keywords:
Collagen assay
Desmoplasia
Ion channel
Oncochannelopathy
Tumor fibrosis

ABSTRACT

Rationale: Pancreatic stellate cells (PSCs) produce a collagen-rich connective tissue in chronic pancreatitis and pancreatic ductal adenocarcinoma (PDAC). Ca^{2+}-permeable ion channels such as ORAI1 are known to affect PSC proliferation and myofibroblastic phenotype. However, it is unknown whether these channels play a role in collagen secretion.
Methods: Using the PSC cell line PS-1, we characterized their cell-derived matrices using staining, mass spectroscopy, and cell migration assays. We developed and validated a high-throughput *in vitro* fibrosis assay to rapidly determine collagen quantity either with Sirius Red or, in the optimized version, with the collagen-binding peptide CNA-35-tdTomato. We assessed collagen deposition upon stimulating cells with transforming growth factor β1 (TGF-β1) and/or vitamin C without or with ORAI1 modulation. Orai1 expression was assessed by immunohistochemistry in the fibrotic tumor tissue of a murine PDAC model (KPfC).
Results: We found that TGF-β1 and vitamin C promote collagen deposition from PSCs. We used small interfering RNA (siRNA) and the inhibitor Synta-66 to demonstrate that ORAI1 regulates collagen secretion of PSCs but not NIH-3T3 fibroblasts. Physiological levels of vitamin C induce a drastic increase of the intracellular [Ca^{2+}] in PSCs, with Synta-66 inhibiting Ca^{2+} influx. Lastly, we revealed Orai1 expression in cancer-associated fibroblasts (CAFs) in murine PDAC (KPfC) samples.
Conclusion: In conclusion, our study introduces a robust *in vitro* assay for fibrosis and identifies ORAI1 as being engaged in PSC-driven fibrosis.

Introduction

Pancreatic ductal adenocarcinoma (PDAC) is the most common malignant tumor of the exocrine pancreas. Pancreatic cancer has one of the poorest prognoses among all cancers with a 5-year survival rate of 13 % [1]. A hallmark of PDAC is the development of a collagen-rich, fibrotic stroma, also referred to as desmoplasia. The fibrotic extracellular matrix (ECM) itself promotes cancer growth, invasion, metastasis formation, and chemotherapy resistance [2–4]. Thus, there is a negative correlation between ECM deposition and patient survival [5]. In PDAC, specific matrix components are overrepresented, such as type VI collagen, fibrillin-1, or periostin [6]. The ECM not only serves as a rigid scaffold but also exhibits cues that impact cellular behavior. Collagens in the ECM interact with integrins in the plasma membrane of pancreatic cancer cells and promote their proliferation and migration [7]. In addition, the fibrotic stroma creates a barrier around the tumor, hampering therapeutical drug delivery and thereby contributing to therapy failure [8]. For these reasons, the tumor stroma is viewed as a potential therapeutic target [9].

However, the role of fibrotic stroma in terms of tumor growth and prognosis is not unambiguous. *In vivo,* mouse studies revealed that the total depletion of myofibroblasts, accompanied by reduced type I collagen levels and altered ECM organization, resulted in an invasive tumor phenotype and reduced animal survival [10]. Similar results were found when type I collagen in myofibroblast in PDAC mouse models was downregulated [11]. Deleting Sonic Hedgehog, a ligand driving desmoplasia, resulted in undifferentiated and more aggressive PDAC in mouse models [12]. Clinical trials investigating an additional benefit of Hedgehog inhibitors in combination with the chemotherapeutic agent gemcitabine were halted due to a lack of efficacy [13]. Hence, despite

* Corresponding author.
E-mail address: pethoe@uni-muenster.de (Z. Pethő).

https://doi.org/10.1016/j.matbio.2024.12.004
Received 3 July 2024; Received in revised form 22 November 2024; Accepted 8 December 2024
Available online 9 December 2024

numerous studies, the significance of fibrosis development in pancreatic cancer is still not fully elucidated.

The main drivers of PDAC fibrosis are pancreatic stellate cells (PSCs) and diverse cancer-associated fibroblasts (CAFs). When contributing to tumor fibrosis, these cells upregulate alpha-smooth muscle actin (αSMA) expression and adopt a myofibroblast-like shape [3,14,15]. Besides secreting an abundance of collagens and other ECM proteins, PSCs orchestrate the alignment of collagen fibers in the tumor stroma [16]. Collagen fiber alignment promotes pancreatic cancer cell migration and invasion through contact guidance [17]. One of the most significant growth factors in PSCs in PDAC is the transforming growth factor β1 (TGF-β1) [18,19]. TGF-β1 enhances PSC proliferation, migration, and ECM protein deposition [20]. PSCs are not only TGF-β1 responsive but also secrete high amounts of this protein. Besides TGF-β1, vitamin C is another essential component for ECM synthesis. As a redox cofactor, it allows the hydroxylation of proline and lysine residues, facilitating collagen triple helix assembly. In addition, vitamin C significantly stimulates the proliferation of fibroblasts and collagen expression [21,22]. Interestingly, vitamin C has been demonstrated to regulate membrane receptors and ion channels, and these activities are directly or indirectly linked with calcium ions [23]. In cancer, vitamin C may participate in cellular Ca^{2+} homeostasis and can induce Ca^{2+} influx, e.g., into retinoblastoma and laryngeal carcinoma cells [24,25].

TGF-β1 secretion of PSCs depends on the function of ion channels such as the Ca^{2+}channel ORAI1 [26]. Moreover, ORAI1 is crucial in PSC activation, proliferation, and migration [27]. In addition, ORAI1 promotes fibroinflammatory gene expression in PSCs [28]. Furthermore, Orai1 inhibition prevents the progression of early chronic pancreatitis *in vivo* in mice [27]. Based on these findings, we hypothesized that ORAI1 is involved in PDAC fibrosis.

As ORAI1 is a Ca^{2+} channel, and intracellular [Ca^{2+}] is key in exocytotic processes [29], we postulated that ORAI1 mediates collagen release and deposition from PSCs in PDAC. A crucial precondition for addressing this hypothesis would be a sensitive, high-throughput fibrosis assay specifically for PSCs, which – to the best of our knowledge – does not exist to date. Therefore, we aimed to establish a new *in vitro* assay for pancreatic fibrosis. Then, using this tool, we assessed and mechanistically dissected the involvement of ORAI1 in PSC-mediated collagen secretion.

Results

High-throughput in vitro fibrosis assay for quantifying collagen secretion of PSCs

For addressing a potential role of ORAI1 in pancreatic fibrosis, we first developed a high-throughput PSC fibrosis assay using the human pancreatic stellate cell line PS-1 [30]. Initially, we designed the 96-well plate-based fibrosis detection assay based on the fact that Sirius Red binds to basic amino acids and thereby detects extracellular matrix proteins [31,32]. We validated the assay using collagen standards and found the detection limit of the assay to be ~ 0.1 mg/ml collagen I, above which Sirius Red absorbance follows a linear regression (Supp. Fig. 1). PS-1 cells deposit a thick, contiguous layer of ECM over ten days (Fig. 1B). Matrix secretion is especially prominent when PSCs are stimulated with 10 ng/ml TGF-β1 and 50 μg/ml (284 μM) vitamin C (Fig. 1A-C, Supp. Fig. 2). The sigmoidal pattern of Sirius Red absorbance over time implies that PS-1 cell-derived matrix deposition saturates after 10 days (Fig. 1C).

As mentioned above, a limitation of Sirius Red is that it is not specific for collagens, as it also detects basic amino acids of other cellular and ECM proteins [33]. This was reflected in our assay setting by the socalled Z' factor (Z prime factor) [34], which turned out to be Z'=−0.60. This negative value implies that the assay setting is not suitable for high-throughput screening. Thus, we set out to obtain a more specific readout regarding the collagen quantity. Collagens are the most abundant constituents of the PDAC ECM, and multiple collagens are associated with PDAC progression and prognosis [6].

We assessed the quality of decellularized matrices by immunostaining using a collagen I (COL1A2) antibody as well as the collagen-binding peptide CNA-35-tdTomato (Fig. 1D). These stainings confirm the presence of collagens in the fibrillar PS-1 cell-derived ECM. Moreover, using confocal microscopy, we measured that CNA35-tdTomato-stained matrices have a thickness of 18.5 ± 2.3 μm ($N = 3$ independent experiments), confirming their three-dimensional nature of the ECM. Complementary to immunofluorescence, we assessed the collagen content of the PS-1 cell-derived ECM using Western blotting (Fig. 1E). Indeed, decellularized matrices, secreted by PS-1 cells over 7 days, contain mature collagens. In contrast, PS-1 whole cell lysates contain only procollagens but no mature collagens. Furthermore, the matrix produced by PS-1 cells contains numerous other proteins as detected by Coomassie staining (Fig. 1F). We assessed the qualitative composition of the matrix with mass spectroscopy (Supp. Table 1). The main constituents of the matrix are collagens and glycoproteins, similar to previously reported ECM constituents in the pancreas and PDAC [6].

Using fluorescence microscopy, we observed that CNA-35-tdTomato produces more vibrant images than Sirius Red when assessing fibrillar collagen (Fig. 1D). Accordingly, CNA-35-tdTomato has an approximately 6-fold signal increase upon PS-1 cell stimulation with 10 ng/ml TGF-β1 and 284 μM vitamin C, as compared to a 3-fold signal increase with Sirius Red (Fig. 1G). This indicates that CNA-35-tdTomato is superior to Sirius Red in detecting PS-1 cell-derived collagen in a plate-based assay. Moreover, the Z' factor amounts to Z'=0.30 for the CNA-35-tdTomato-based assay indicating a substantial improvement of the assay quality as compared to the Sirius Red-based assay. It can now be applied in a high-througput setting. Additionally, CNA-35-tdTomato offers more technical flexibility than Sirius Red, as decellularization is no longer necessary because of its much higher sensitivity and specificity. Therefore, we used CNA-35-tdTomato staining as the primary readout of the subsequent experiments.

PS-1 cell-derived matrices regulate PDAC cell migration behavior

The biochemical characteristics of the PS-1 cell-derived matrix seemed indeed promising as a PDAC fibrosis model, as it recapitulates properties of the ECM in PDAC. Next, we tested the physiological quality of the PS-1 cell-derived matrix. Studying the response of cells plated onto cell-derived matrices is a common way to validate the quality and functionality of the cell-derived matrix model [35,36]. For this, we compared the migratory behavior and morphological characteristics of the human PDAC cell line Panc-1 seeded onto uncoated tissue culture-treated dishes versus an artificial reconstituted *in vitro*-polymerized ECM [37–39] or a decellularized PS-1 cell-derived matrix (Fig. 2A).

Panc-1 cells seeded onto uncoated dishes perform a negligible amount of random cell migration in an undirected manner (Fig. 2B-C). In contrast, Panc-1 cells seeded onto the cell-derived matrix move with a much higher persistence along the ECM fibers – as evidenced by the distribution of the step-by-step turning angles between each time interval (Fig. 2B-C, Supplementary Videos 1–3). This persistent migration behavior defined by a preferential adhesion to the aligned substrate is also known as haptotaxis. Cell persistence is in direct contrast to the behavior of Panc-1 cells migrating on an unaligned, reconstituted ECM (Fig. 2D). Hence, the translocation of Panc-1 cells on the PS-1 cell-derived matrices is higher (Fig. 2E). Cell migration velocity does not differ between Panc-1 cells seeded onto a PS-1 cell-derived matrix and those seeded on an artificially reconstituted matrix (Fig. 2F). Thus, the migration "motor" of Panc-1 cells appears not to be affected by these different matrices.

Cell shape mirrors the migratory behavior. Panc-1 cells migrating on the PS-1 cell-derived matrix have a more elongated morphology that is aligned with the matrix fibers (Fig. 2A, G). In contrast, Panc-1 cells

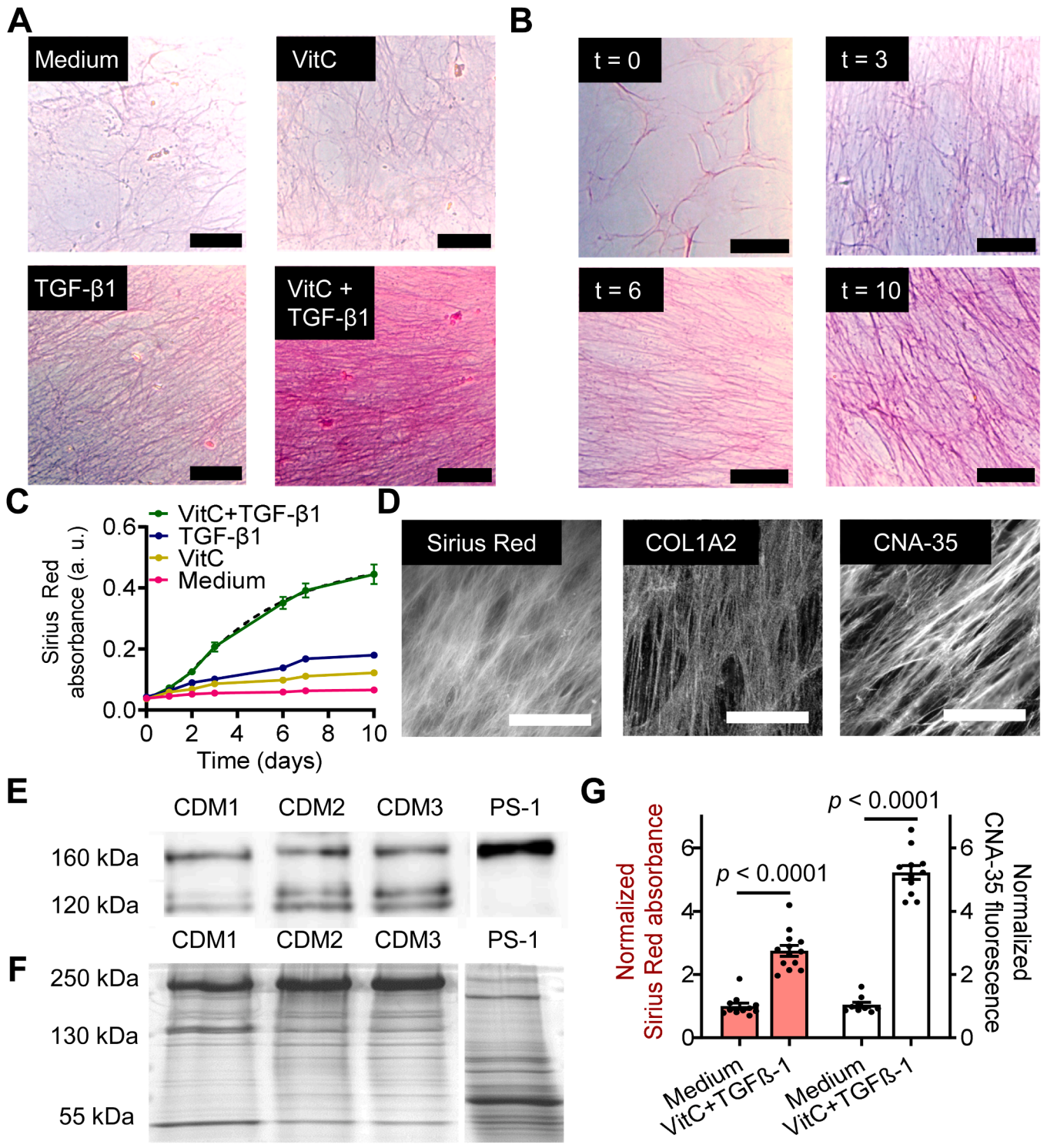

Fig. 1. PS-1 cells produce a dense collagen-based extracellular matrix.
(A) Exemplary brightfield images of decellularized PS-1 cell-derived ECM without stimulation (Medium), and upon stimulation with 284 μM vitamin C (VitC), 10 ng/ml TGF-β1 (TGF-β1) and combined 284 μM vitamin C and 10 ng/ml TGF-β1 stimulation (VitC + TGF-β1), acquired at $t = 7$ days. Scale bar = 50 μm. (B) Time-dependence of PS-1 cell-derived ECM deposition upon stimulation with 284 μM vitamin C and 10 ng/ml TGF- β1, acquired directly after starting the stimulation ($t = 0$) and after $t = 3$d, 6d, and 10d Scale bar = 50 μm. (C) Time course of PS-1 cell-derived ECM deposition after treatments detailed in (B). The quantity of deposited matrices was measured at time points $t = 0$; 1; 2; 3; 6; 7; and 10 d, using Sirius Red absorbance as readout (N/n = 3–6 independent experiments, with 12–18 matrices per data point). The dashed line indicates a sigmoidal curve fit. (D) Representative fluorescence images of decellularized matrices after Sirius Red (left), COL1A2 (middle), and CNA-35-tdTomato (right) labeling ($N = 3$). Scale bar = 50 μm. (E) Western blots of COL1A2 from PS-1 cell-derived ECMs (cell-derived matrices CDM 1–3, $N = 3$) compared to PS-1 whole cell lysate. Bands appear at the theoretical molecular mass of immature α2 procollagen (160 kDa) and mature α2 (120 kDa) collagen. (F) Coomassie staining of PS-1 cell-derived ECM and PS-1 cell lysate-containing gel after electrophoresis, showing numerous protein bands. (G) Scatter bar plot shows the sensitivity of Sirius Red absorbance (left) versus CNA-35-tdTomato fluorescence (right), as readouts to quantify PS-1 cell-derived ECM deposition. The absorbance and fluorescence at $t = 7$ d were normalized to the mean of the decellularized PS-1 cell-derived ECM without stimulation (Medium) (N/n = 3 individual experiments / 9–11 cell-derived matrices). Data in (C) and (G) are displayed as mean±SEM with statistical comparison in (G) using Student's t-test.

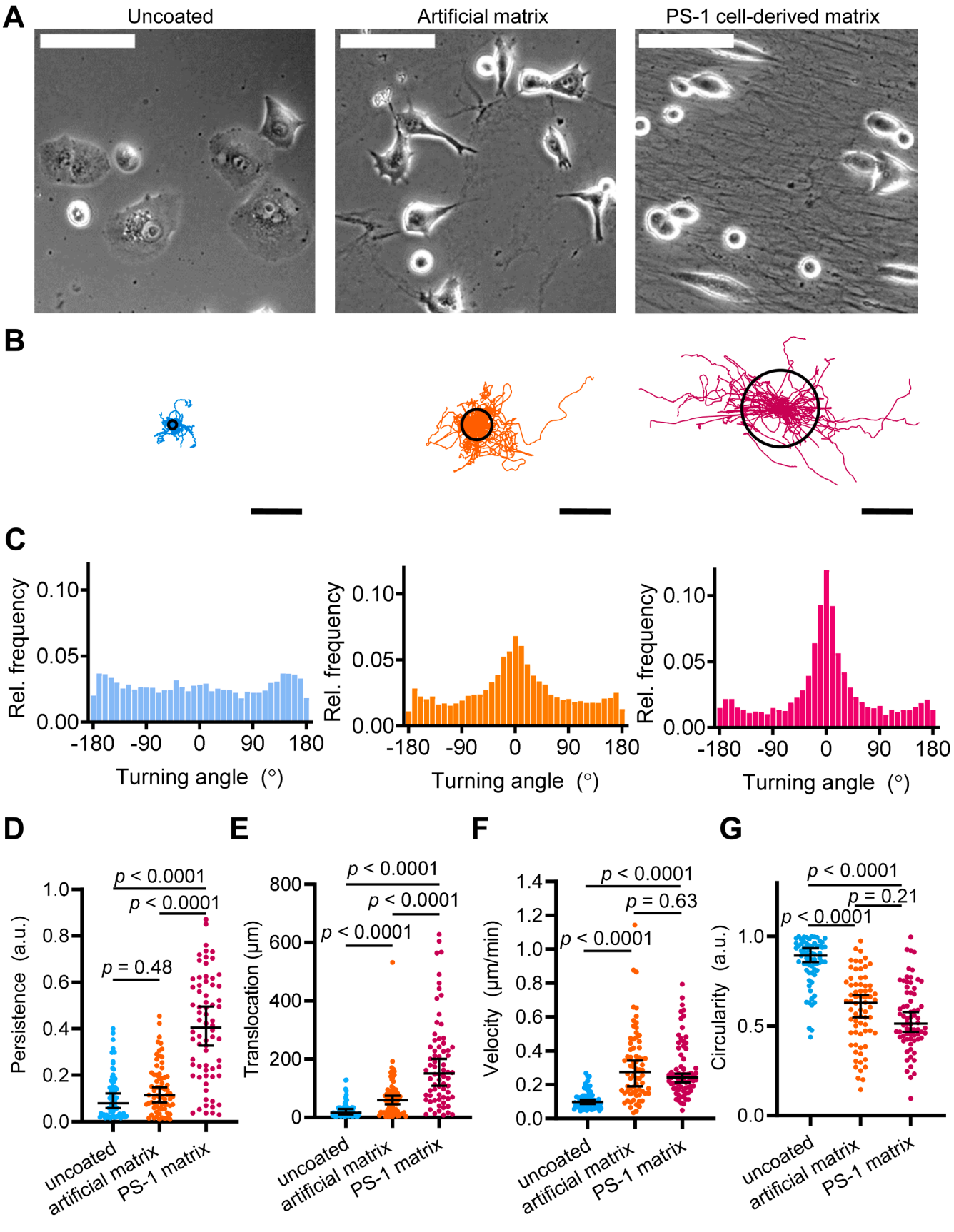

(caption on next page)

Fig. 2. The PS-1 cell-derived matrix impacts the migratory properties of Panc-1 cells.
(A) Representative phase contrast images depict Panc-1 cells migrating in uncoated tissue-culture flasks (left), on an artificial reconstituted matrix (middle), and on a decellularized PS-1 cell-derived matrix (right). Scale bar = 100 μm. (B) Trajectories of individual Panc-1 cells normalized to common starting points. Cells were migrating on an uncoated substrate (blue, left), reconstituted artificial ECM (orange, middle), and decellularized PS-1 cell-derived matrix (magenta, right) for 24 h The diameter of the black circles indicates the median start-to-end translocation of Panc-1 cells, detailed in (E). Scale bar 200 μm. ($N = 4$ independent experiments / $n = 70$ cells). (C) The relative frequency of turning angles, calculated relative to the previous time interval of the migration trajectories depicted in (B), were determined at each time point for each Panc-1 cell, then binned in 10° steps to assess the level of migratory persistence, further detailed in (D). (D-G) Scatter plots depict the quantification of cell migration parameters: persistence (D), translocation (E), velocity (F), and circularity (G). Data points in (D-G) are displayed as median and 95 % confidence interval, with a statistical comparison performed using the Kruskal-Wallis test with Dunn's post-hoc test.

migrating on uncoated dishes are more circular. The data above indicates that the PS-1 cell-derived matrix promotes persistent Panc-1 cell migration, which underlines the physiological relevance of this model system.

Vitamin C stimulates collagen exocytosis from PSCs and induces Ca^{2+}entry

Having developed the appropriate model system and assay setup, we mechanistically dissected collagen release and deposition from PS-1 cells. Above, we observed that 10 ng/ml TGF-β1 as well as 284 μM vitamin C stimulate ECM deposition (Fig. 1C). Thus, we investigated the impact of vitamin C and TGF-β1 on collagen release by detecting intracellular collagen using CNA-35-tdTomato in permeabilized PS-1 cells. Upon treating PS-1 cells with 10 ng/ml TGF-β1, 284 μM vitamin C, or their combination, we observed distinct cellular distributions of collagen. To qualitatively estimate the differences, we established a scoring system where a higher score indicates a more advanced/pronounced collagen release of intracellular collagen molecules to extracellular fibers (Fig. 3A). Unstimulated PS-1 cells display either no distinct collagen signal (score 0) or a perinuclear signal (score 1) (Fig. 3B). Treatment with 10 ng/ml TGF-β1 exhibits an enhanced perinuclear signal, indicating that TGF-β1 drives perinuclear collagen accumulation indicative of increased collagen synthesis. In contrast, vitamin C drives collagen exocytosis, as evidenced by the presence of extracellular collagen fibers (score 3). The highest amounts of collagen accumulation in the cell periphery (score 2), and collagen release were found upon stimulation of both collagen synthesis and release, using 10 ng/ml TGF-β1 and 284 μM vitamin C in combination (Fig. 3C). To investigate how fast PS-1 cells respond to vitamin C, we compared 284 μM vitamin C added for only 1 h, to overnight 284 μM vitamin C treatment, in TGF-β1-pretreated PS-1 cells. Collagen accumulates in the cell periphery already after 1 h vitamin C addition (Fig. 3B-C). The data above shows that vitamin C mediates collagen release by inducing peripheral collagen accumulation and exocytosis.

Given that collagen secretion occurs by exocytosis [29] — which in itself is a Ca^{2+}-regulated process — we hypothesized that vitamin C influences exocytosis through Ca^{2+}. Vitamin C could either be involved indirectly via Ca^{2+} signaling molecules or directly by eliciting Ca^{2+} signals. First, we tested whether vitamin C elicits Ca^{2+} signals itself by performing intracellular Ca^{2+} measurements on PS-1 cells (Fig. 3D). Here, we found a striking, concentration-dependent increase of the intracellular [Ca^{2+}] of PS-1 cells, already prominent after 284 μM vitamin C treatment, and further increased using 1 mM vitamin C (Fig. 3E, Supp. Fig. 3). However, it is known that vitamin C quenches the fluorescence of acriflavine [40] and anthocyanin [41] by a redox reaction. To ascertain that our observations are not artifacts due to a redox interaction between the Ca^{2+}-sensitive dye Fura-2 and vitamin C, we tested whether different concentrations of vitamin C affect the fluorescent properties of Fura-2 in a cuvette (Fig. 4F). Here, we found that the spectrum of Fura-2 is not affected by vitamin C in the concentration range of 1 μM - 1 mM. Thus, we conclude that vitamin C leads to an increased intracellular [Ca^{2+}] in PSCs in a dose-dependent manner.

To test whether vitamin C impacts on Ca^{2+}signaling, we examined the phosphorylation states of the upstream Ca^{2+} signaling molecule, Ca^{2+}/calmodulin-dependent protein kinase II (CaMKII), and the downstream transcription factor cAMP response element-binding protein (CREB) at various time points after vitamin C stimulus (Fig. 3G). Despite the significant changes in collagen exocytosis that we presented above (Fig. 3B-C), neither CaMKII nor CREB phosphorylation were affected by vitamin C stimulation (Fig. 3H).

Vitamin C elicits Ca^{2+} entry into PSCs

Following up on the finding that vitamin C elicits an increase in intracellular [Ca^{2+}], we next investigated where Ca^{2+} ions originate from. Here, we focused on the ORAI1 channel as it is a key ion channel in the activation, proliferation, and migration of PSCs through enabling Ca^{2+} influx [27]. First, we investigated the impact of vitamin C (284 μM) on the $[Ca^{2+}]_i$ in the absence of extracellular Ca^{2+}(Fig. 4A). Under these conditions, vitamin C fails to increase the $[Ca^{2+}]_i$ in PS-1 cells (Fig. 4B). However, when we proceed to superfuse PS-1 cells with Ca^{2+}-containing Ringer's solution supplemented with vitamin C, the $[Ca^{2+}]_i$ drastically increases. This implies that vitamin C triggers Ca^{2+} influx from the extracellular space. To assess Ca^{2+}entry further, we used the Mn^{2+} quench assay [37,42,43]. Here, increased Fura-2 quenching by Mn^{2+} entry is a surrogate of increased Ca^{2+} influx. We found that vitamin C leads to a drastic Mn^{2+}entry into PS-1 cells, which would correspond to a marked Ca^{2+}influx (Fig. 4C-D). We observed the same effects when pretreating PS-1 cells with 284 μM vitamin C for 24 h Moreover, the rate of Mn^{2+}entry decreases upon treatment with the ORAI1 inhibitor Synta-66 (10 μM) but does not reach the baseline level. Our findings suggest that vitamin C induces Ca^{2+}-entry within minutes independently of a pretreatment, likely via a direct effect on an ion channel. Furthermore, the data indicate that calcium ions responsible for the vitamin C-dependent $[Ca^{2+}]_i$ increase mainly originate from the extracellular space.

The finding that there is still significant Mn^{2+}entry into PS-1 cells upon ORAI1 inhibition using 10 μM Synta-66 implies that Ca^{2+}does not exclusively enter the cells through ORAI1. To ascertain this observation, we performed Mn^{2+} quench experiments in si*ORAI1* PS-1 cells (Fig. 4E). *ORAI1* small interfering RNA (siRNA) reduces *ORAI1* expression in PS-1 cells by approximately 75 % compared to PS-1 cells treated with scrambled siRNA as determined by qPCR. PS-1 cells also express *ORAI2* and *ORAI3,* and the expression of these genes is not affected by si*ORAI1* treatment (Supp. Fig. 4). We found that there is no difference between the vitamin C-induced Mn^{2+}entry of PS-1 cells treated with si*ORAI1* siRNA compared to the scrambled siRNA control (Fig. 4E). This finding implies that vitamin C-elicited Ca^{2+}influx is likely not primarily through ORAI1.

From the results above, it remained unclear whether vitamin C-induced Ca^{2+} entry, blockable by Synta-66, is cell line-specific or a general phenomenon. To provide a broader basis for our findings, we included primary murine PSCs (mPSCs) and the embryonic mouse fibroblast cell line NIH-3T3 as additional cell types in our study (Fig. 4G-J). Vitamin C induces Ca^{2+}influx into primary PSCs (Fig. 4G-H) but not into NIH-3T3 cells (Fig. 4I-J). This indicates a distinct response to vitamin C in PSCs compared to NIH-3T3 fibroblasts. 10 μM Synta-66 impairs Mn^{2+}entry in primary PSCs (Fig. 4H), suggesting that Ca^{2+} influx mechanisms are comparable in the human PSC cell line PS-1 and primary murine PSCs. However, the amplitude of vitamin C-elicited Ca^{2+} influx in human PS-1 cells is higher than that of murine PSCs. This

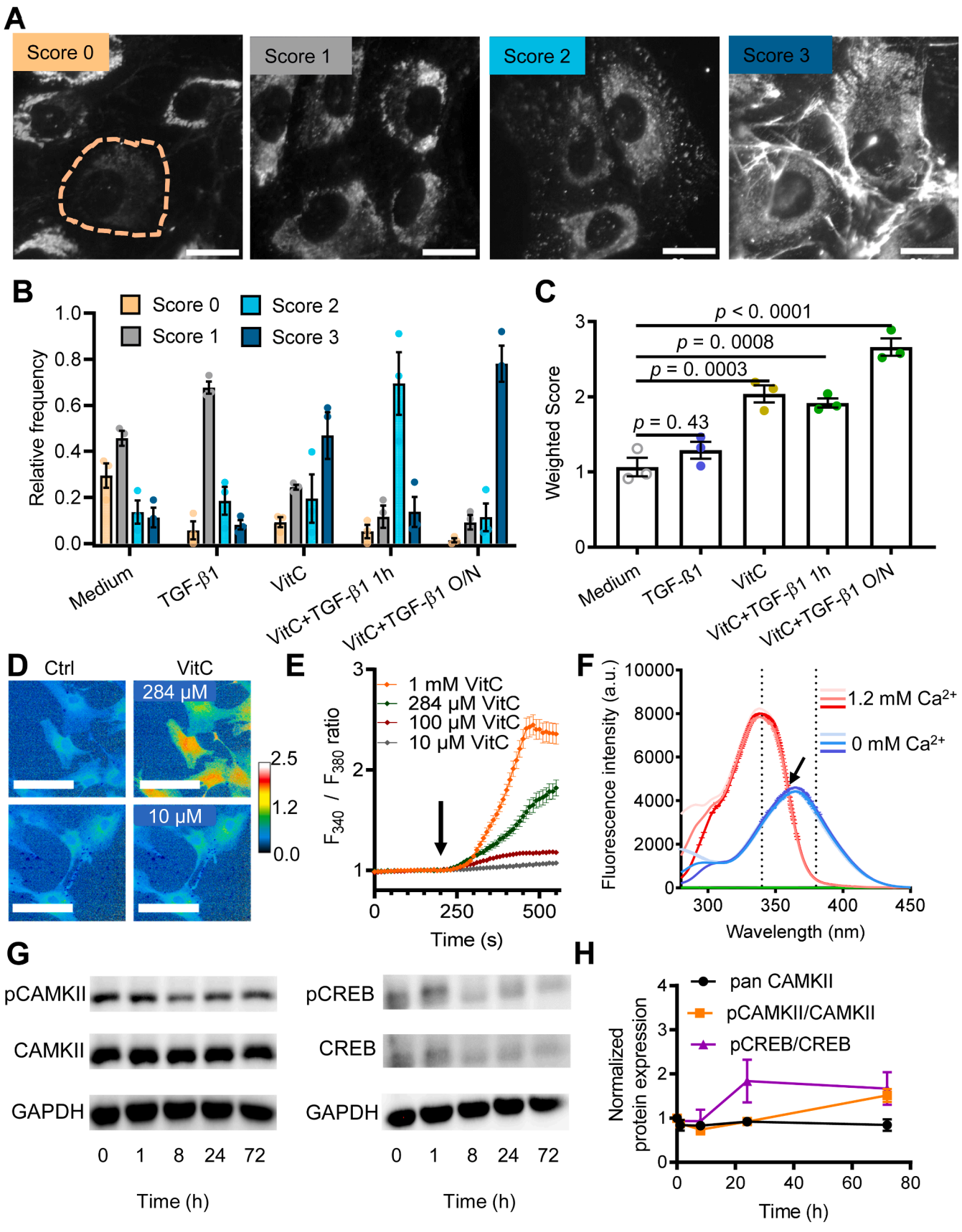

(caption on next page)

Fig. 3. Vitamin C mediates collagen exocytosis and causes an increase of the $[Ca^{2+}]_i$ in PS-1 cells.
(A) Representative fluorescence images of fixed and permeabilized PS-1 cells labeled with CNA35-tdTomato. Single-cell fluorescence images visualizing intracellular and extracellular collagen fiber deposition in detail are examples of the established scoring system. Score 0: marginal signal of intracellular collagen; Score 1: perinuclear collagen accumulation; Score 2: peripheral collagen accumulation distributed throughout the entire cytoplasm; Score 3: extracellular collagen fibers. Scale bar = 20 μm. (B) The scatter plot depicts the relative frequency of matrix deposition scores of PS-1 cells without stimulation (Medium), 284 μM vitamin C (VitC) and 10 ng/ml TGF-β1 (TGF-β1) for 24 h each, or combination treatment for 1 h, or overnight (O/N), (N / n = 3 independent experiments / n = 3 means of individual data points). (C) The diagram shows the weighted scores of data presented in (B), allowing statistical comparison of collagen release between different treatments. (D) Pseudocolored F_{340}/F_{380} ratio images correlating with the intracellular $[Ca^{2+}]$ of PS-1 cells upon control superfusion (left panel, Ctrl) and after superfusion with 284 μM vitamin C (top) or 10 μM vitamin C (bottom). (E) Quantification of vitamin C superfusion on the F_{340}/F_{380} ratio over time at different concentrations, i.e., 10 μM (grey), 100 μM (brown), 284 μM (green), 1 mM (orange). Vitamin C superfusion starts at t = 200 s as indicated by the black arrow. (N /n = 3 independent experiments / n = 41–61 cells). (F) Fluorescence intensities at different excitation wavelengths reveal the excitation spectra of Fura-2 dissolved in Ringer's solution (1.2 mM Ca^{2+}, red) or Ca^{2+}-free Ringer's solution (0 mM Ca^{2+}, blue) without vitamin C (light), with 284 μM vitamin C (medium), or with 1 mM vitamin C (dark). Under the same settings, the spectrum of 10 mM vitamin C without Fura-2 is depicted in green. A black arrow indicates the isosbestic wavelength of Fura-2. Dashed lines at l = 340 nm and l = 380 nm indicate the excitation wavelengths used for the ratiometric measurements (N / n = 3 experiments / n = 3 replicates). (G) Representative Western blots of phospho-CAMKII (p-CAMKII, top, left) versus pan-CAMKII (CAMKII, middle, left), and phospho-CREB (p-CREB, top, right) versus pan-CREB (CREB, middle, right), compared to the respective GAPDH bands (bottom) at t = 0; 1; 8; 24; 72 h (H) The diagram depicts the quantitative evaluation of the Western blot bands, normalized to GAPDH, over time (N / n = 3 experiments / n = 3 replicates). Data points are displayed as mean±SEM, with statistical comparison in (C) performed using one-way ANOVA with Tukey's post-hoc test.

differential response across species may be attributed to the inability of human cells to synthesize vitamin C in contrast to murine cells [44]. Surprisingly, Synta-66 (10 μM) does not inhibit but rather augments the Ca^{2+}influx into NIH-3T3 cells (Fig. 4J). As ORAI2 is known to be activated by Synta-66, and ORAI3 is not affected by Synta-66 at all [45], this result may hint at Orai2 in NIH-3T3 fibroblasts. In summary, we found that ORAI1 may not be a key player in vitamin C-elicited Ca^{2+}influx.

ORAI1 regulates collagen release in PSC-derived matrices

After elucidating the mechanistic details of vitamin C-elicited Ca^{2+} response and finding that ORAI1 does not play a key role in that process, we tested our original hypothesis that ORAI1 regulates collagen release and deposition from PSCs. To evaluate the role of ORAI1 in collagen release, we applied CNA-35-tdTomato labeling. Indeed, the staining with CNA-35-tdTomato of non-permeabilized PS-1 cell culture allowed the detection of extracellular fibrillar collagen after 24 h, both qualitatively (Fig. 6A, C) and quantitatively (Fig. 6B, D). To minimize dye internalization, the staining duration was shortened to 20 min. We inhibited Ca^{2+} influx using the small-molecule inhibitor Synta-66 and employed a siRNA-based approach to silence *ORAI1* expression. As expected, stimulation with 10 ng/ml TGF-β1 and 284 μM vitamin C markedly increases collagen release of PS-1 cells after 24 h (Fig. 6A-B). Importantly, VitC + TGF-β1 fails to induce collagen release in si*ORAI1*-treated PS-1 cells. Moreover, 10 μM Synta-66 significantly reduces collagen release of PS-1 cells treated with scrambled siRNA but not when treated with si*ORAI1* (Fig. 6B). To distinguish whether the inhibitory effects of Synta-66 are due to the inhibition of vitamin C or TGF-β1 stimulus, we investigated them individually. Our data confirms that especially vitamin C facilitates collagen release, which is impaired by 10 μM Synta-66 (Supp. Fig. 5). These data indicate that ORAI1 together with vitamin C are regulators of collagen release from the human PSC cell line PS-1.

Similarly to PS-1 cells, stimulation with 10 ng/ml TGF-β1 and 284 μM vitamin C markedly increases collagen release from mPSCs and NIH-3T3 fibroblasts (Fig. 6C-D). Moreover, the ORAI1 inhibitor 10 μM Synta-66 reduces collagen release from primary murine PSCs. In contrast, the collagen release from NIH-3T3 cells is not affected by 10 μM Synta-66. These data imply that the treatments affect collagen release differentially in different cell types, which is in line with our mechanistic findings in the Mn^{2+} quench assay (Fig. 5). Whenever Synta-66 reduces Ca^{2+} influx, collagen secretion is also reduced. However, in NIH-3T3 fibroblasts, the inhibitory effect of Synta-66 appears to be overridden, e.g., by activation of Orai2 channels [45]. An alternative explanation could be that the different treatments affect cell viability, consequently affecting collagen release. To exclude this possibility, we assessed cell viability by measuring cellular ATP content. We found that cells have similar viability under all conditions, indicating that neither 10 μM Synta-66 nor si*ORAI1* impair cell viability (Fig. 6E).

The observed effects of Synta-66 were seen within 24 h Yet, pancreatic fibrosis evolves over a much longer time course. To assess collagen deposition over a longer time in vitro, we determined the impact of 10 μM Synta-66 on collagen secretion during a 7d period in PS-1 cells. Indeed, collagen accumulation is significantly decreased when PS-1 cells stimulated with 10 ng/ml TGF-β1 and 284 μM vitamin C are treated additionally with 10 μM Synta-66 (Fig. 6F) over one week.

Our findings suggest that ORAI1 is involved in the collagen release of murine and human PSCs. On the other hand, ORAI1-regulated collagen release is not a general phenomenon applicable to all fibroblasts and may be overridden by other mechanisms. Accordingly, Synta-66 has no effect on the collagen release from the fibroblast cell line NIH-3T3.

ORAI1 is present in cancer-associated fibroblasts in fibrotic PDAC

After pointing out that ORAI1 is involved in collagen release from PSCs, we aimed at investigated the relevance of this finding in PDAC fibrosis. Therefore, we measured Orai1 protein expression in pancreatic cancer *in situ,* using tissue slices from genetically engineered KPfC mice that harbor a heterozygous loss of p53 and conditionally express mutant K-Ras (genotype $Kras^{wt/LSL-G12D}$ $Tp53^{fl/+}$ $PDX1\text{-}Cre^{+}$). We assessed Orai1 by immunohistochemistry in murine KPfC tissue sections (Fig. 1A-B, Supp. Fig. 6) that contain numerous tumor nodes as well as neighboring non-tumorous pancreatic tissue. We detected a punctate Orai1 staining pattern in PDAC, primarily in αSMA^{+}cancer-associated fibroblasts. Moreover, the vessel-lining endothelial cells express Orai1 in PDAC and in the surrounding non-tumorous pancreatic tissue.

Next, we compared Orai1 expression in non-fibrotic nodes with collagen-rich fibrotic tumor nodes (Fig. 1B). To visualize tumor fibrosis, we used the fluorescently labeled bacterial collagen-binding peptide CNA-35-tdTomato [46,47]. Quantitative histopathology indicates that overall, 25 % of αSMA^{+}cells are $Orai1^{+}$. Intriguingly, $Orai1^{+}$ CAFs are more prevalent in tumor nodes that contain marked fibrosis than in non-fibrotic tumor nodes (Fig. 1C). These findings show that Orai1 is expressed in CAFs in fibrotic PDAC.

Discussion

In this study, we provide evidence for the functional significance of ORAI1 in PSC-driven fibrosis. We gained new insights regarding the role of vitamin C and ORAI1 in PSC collagen release and identified a novel mechanism of vitamin C-induced Ca^{2+} entry. We revealed Orai1 expression predominantly in CAFs within the fibrotic PDAC microenvironment in PDAC *in situ.* Importantly, we present critical methodological innovations to study fibrosis and cell-derived matrices. In

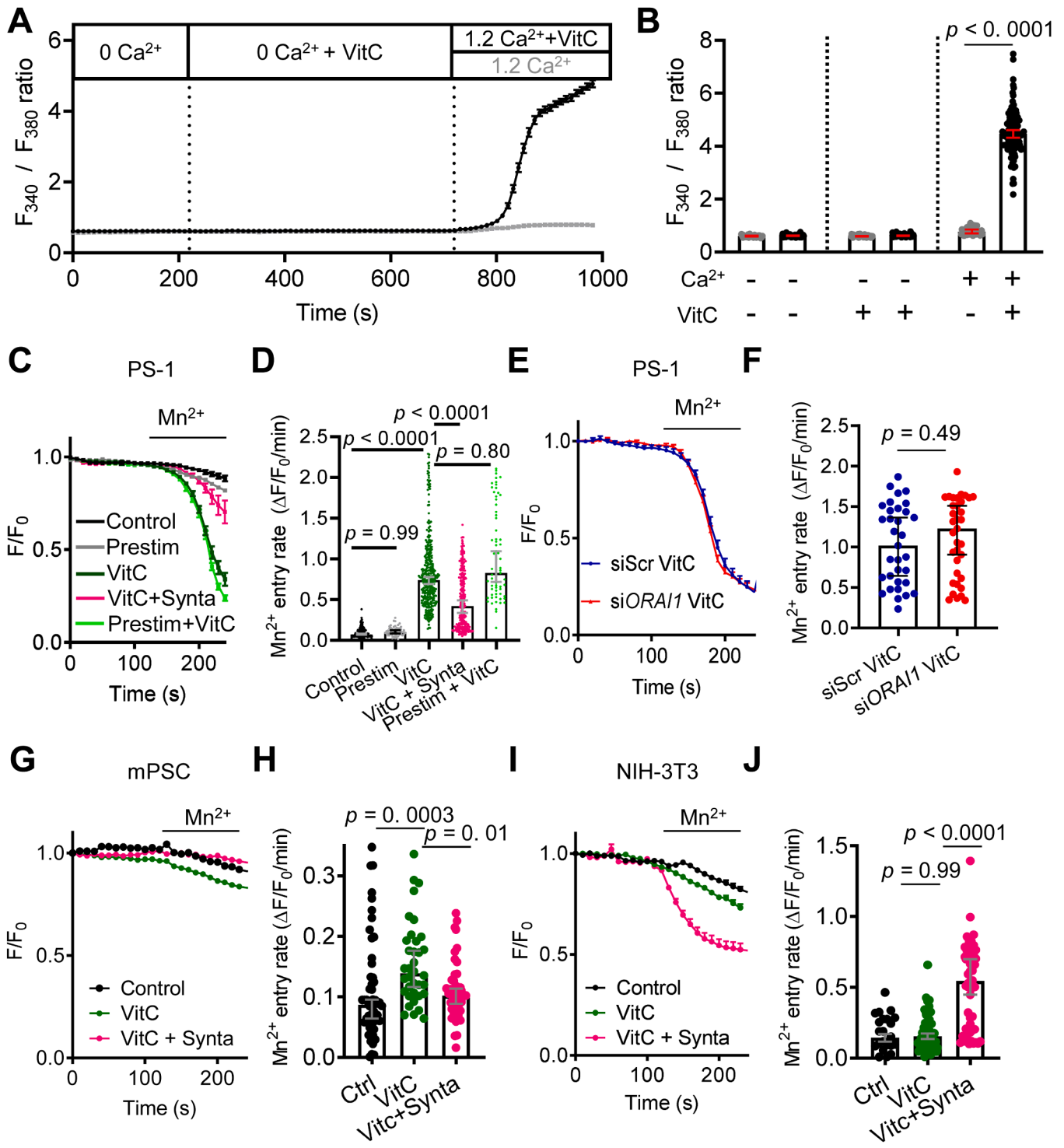

Fig. 4. Ca^{2+}entry after vitamin C treatment can be impaired by Synta-66 in PSCs but not in NIH-3T3 cells.
(A) The $[Ca^{2+}]_i$, here represented by the F_{340}/F_{380} ratio rises when VitC is added to PS-1 cells in the presence of extracellular Ca^{2+} (1.2 mM), but not in the absence of extracellular Ca^{2+}. Dotted lines indicate time points when superfusion solutions were changed. (N / *n* = 4 independent experiments with $n_{1.2\ mM\ Ca2+}$= 45 and $n_{1.2\ mM\ Ca2++VitC}$ = 90 cells). (B) Scatter bar plot shows the quantification of F_{340}/F_{380} ratios under the different experimental conditions. (C-J) Mn^{2+}quench experiments in which the decline of Fura-2 fluorescence is quantified as F/F_0. A steeper slope of the F/F_0 diagrams is indicative of a higher Mn^{2+}influx. This value is depicted as the Mn^{2+}entry rate which is a surrogate of Ca^{2+}influx. The treatments tested were 1 mM Mn^{2+}-Ca^{2+}-free Ringer (Control), in the presence or absence of 284 μM vitamin C (VitC), or 284 μM vitamin C and 10 μM Synta-66 (VitC + Synta). In addition, we tested Mn^{2+}entry into PS-1 cells pretreated with 284 μM vitamin C for 24 h (Prestim). F/F_0 diagrams depict populations of wildtype PS-1 cells (C-D) (N/*n* = 5 independent experiments / *n* ≥ 273 cells), PS-1 cells treated with scrambled siRNA (siScr) and *ORAI1* siRNA (si*ORAI1*) (E-F) (N/*n* = 3 independent experiments / ≥ 19 cells), primary murine PSCs (G-H) (N/*n* = 3 independent experiments / ≥ 36 cells), and NIH-3T3 cells (I-J) (N/*n* = 3 independent experiments / ≥ 27 cells). Data points are displayed as median and 95 % confidence interval, with a statistical comparison performed using the Kruskal-Wallis test with Dunn's post-hoc test.

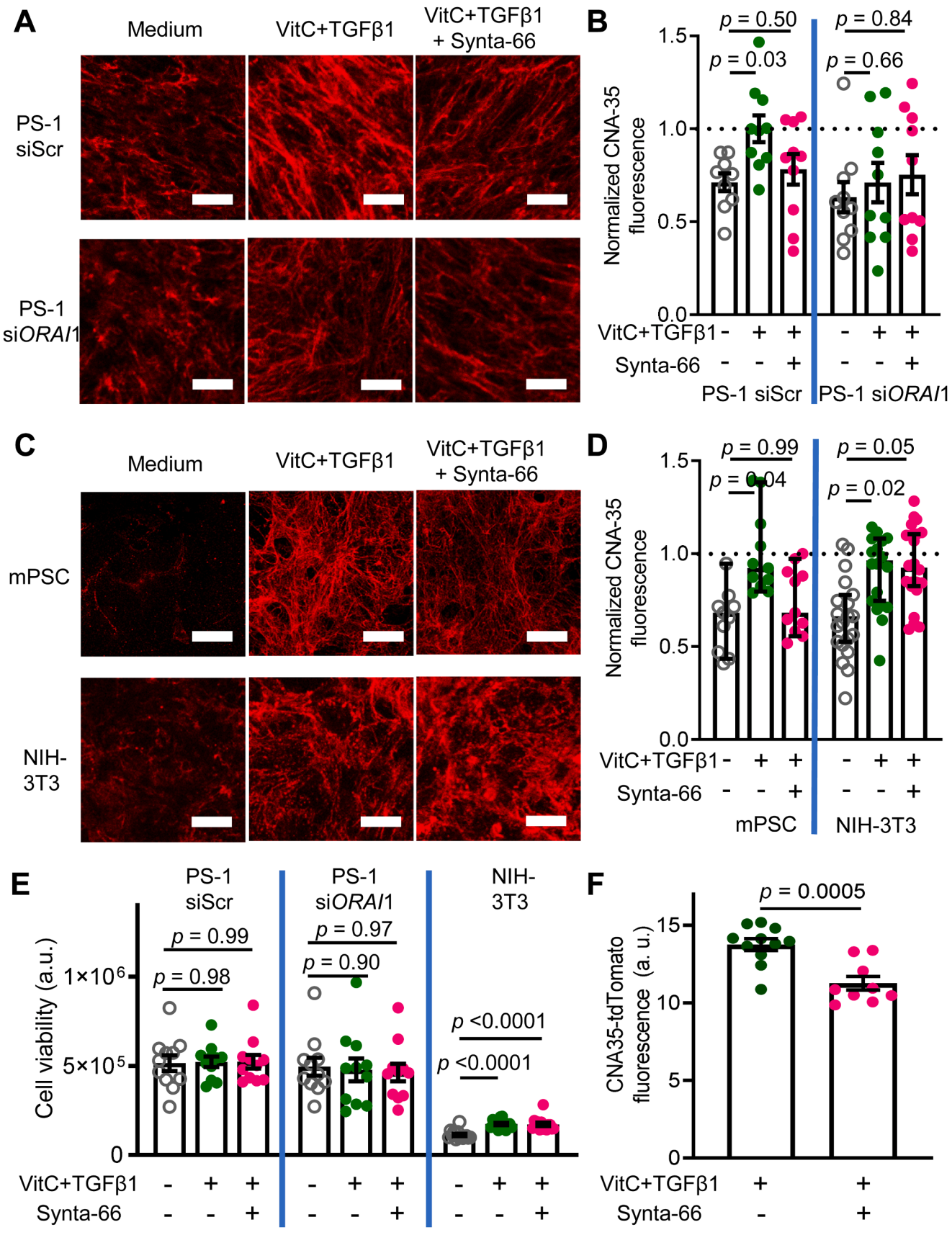

(caption on next page)

Fig. 5. PSC-derived matrix quantity but not cell viability is impaired upon ORAI1 inhibition.
(A) Representative CNA-35-tdTomato fluorescence images of extracellular collagen deposition of PS-1 cells. Cells were transfected with scrambled siRNA (siScr) or siRNA against ORAI1 (si*ORAI1*), and were cultured for 24 h without stimulation (Medium), or with stimulation using 284 μM vitamin C and 10 ng/ml TGF-β1 with 0.1 % DMSO (VitC+TGFβ1), or with 10 μM Synta-66 (VitC+TGFβ1+Synta66). Scale bar = 50 μm. (B) Scatter plot depicts CNA-35-tdTomato fluorescence of cell-derived matrices (depicted in (A)) normalized to the fluorescence intensity of siScr-treated PS-1 cell-derived matrices stimulated with VitC+TGFβ1. Matrices obtained from siScr- and si*ORAI1*-treated PS-1 cells are separated by a vertical blue line. (N/*n* = 3 independent transfections / 10 cell-derived matrices). (C) Representative CNA-35-tdTomato fluorescence images depicting cell-derived matrix structure of primary murine PSCs (mPSCs, top) and NIH-3T3 cells (bottom). Cells were treated as detailed in (A). Scale bar = 50 μm. (D) Scatter plots of CNA-35-tdTomato fluorescence (depicted in (C)) normalized to the fluorescence intensity of matrices obtained from PSCs stimulated with VitC+TGFβ1 (N/*n* = 3 mice with >8 cell-derived matrices); and NIH-3T3 cells (N/*n* = 3 different passages/ >18 cell-derived matrices). Matrices obtained from mPSCs and NIH-3T3 fibroblasts are separated with a vertical blue line. (E) Cell viability per well was quantified using total cellular ATP luminescence, corresponding to data points in (B) for PS-1 cells and to data points in (D) for NIH-3T3 cells. Cell populations are separated with a vertical blue line. (F) The scatter plot depicts a decrease of CNA-35-tdTomato fluorescence when matrix-producing PS-1 cells stimulated with VitC+TGFβ1 are treated with 10 μM Synta-66 for 7 days. (N/*n* = 3 independent experiments / 9 cell-derived matrices). Lines and error bars in all scatter plots except (D) are displayed as mean ± SEM, with statistical comparison performed using Student's *t*-test for (F), and for (B) using one-way ANOVA with Tukey's post-hoc test. Data points in (D) are displayed as median and 95 % confidence interval, with a statistical comparison performed using the Kruskal-Wallis test with Dunn's post-hoc test.

general, cell-derived ECMs are becoming increasingly popular tools to study the involvement of physiologically relevant substrates. Indeed, the PS-1 cell-derived matrix has a composition resembling the pancreatic stroma, with aligned fibers that provide a "railway", resulting in a directional Panc-1 cell migration, also known as haptotaxis [48]. Thereby, our PS-1 cell-derived matrices provide a solid framework for future studies to explore the process and significance of PDAC cell haptotaxis on a pancreas-mimicking substrate.

Despite the considerable advantages of cell-derived matrices over artificially reconstituted matrices, cell-derived matrices are challenging to create and, demand considerable time, effort, and experience in handling, and often ultimately yield a low throughput. We tackled these limitations by harnessing the specificity and sensitivity of CNA-35-tdTomato in detecting collagen. We optimized a 96-well-based assay to study collagen secretion in a qualitative and quantitative manner. Besides assessing collagen accumulation and release in decellularized and even in native samples, CNA-35-tdTomato allowed the assessment of collagen trafficking upon cell permeabilization. CNA-35-tdTomato is highly sensitive and specific compared to traditional fibrosis dyes such as Sirius Red. The fact that CNA-35-tdTomato is a bacterial peptide makes it also cost-effective compared to antibodies. Because of its high sensitivity, CNA-35-tdTomato allows studying cell-derived matrix secretion after only 24 h Thus, experiments are greatly accelerated when compared with existing protocols where collagen accumulation may be needed for over a week [36], prior to detection. Using PS-1 cells, we fine-tuned our assay to study PDAC-like ECM secretion, accumulation, and, subsequently, PDAC cell behavior on the cell-derived matrix. We created a relevant disease-mimicking model for PDAC by stimulating PS-1 cells with vitamin C and TGF-β1. Such a disease-mimicking model may be valuable because of the dire need for translatable approaches for drug screening and development in PDAC [49]. Moreover, our assay is flexible for studying matrix production by other types of fibroblasts.

Applying our *in vitro* assay, we studied the impact of vitamin C on pancreatic fibrosis and showed how vitamin C increases ECM release, and in particular collagen release, from PSCs. Vitamin C is well known for being a cofactor in collagen synthesis and has e.g., also been described to stimulate fibroblast proliferation [21,22]. We, on the other hand, found evidence that vitamin C stimulates collagen release from PSCs. Since exocytosis is often a Ca^{2+}-regulated process, we hypothesized that vitamin C influences collagen exocytosis through Ca^{2+}. Indeed, we could reveal that vitamin C induces a Ca^{2+} influx into PS-1 cells as well as into murine PSCs. Even though the exact mechanisms of vitamin C-regulated Ca^{2+} entry remain unclear, the oxidoreductive properties of vitamin C can provide a plausible explanation. Notably, ORAI1 is redox-sensitive [50], and numerous other ion channels are affected by vitamin C and its metabolites, namely voltage-gated Ca^{2+} channels, NMDA-receptors, and various TRP channels [23]. Thereby, vitamin C would regulate Ca^{2+}-permeable channels to enable Ca^{2+} entry.

Based on the literature, several potential mechanisms are conceivable downstream of the vitamin C-induced Ca^{2+} influx into PSCs that could potentially result in collagen release: (i) Ca^{2+} influx can modulate the cytoskeletal dynamics required for vesicle movement towards the plasma membrane, analogous to Ca^{2+}-mediated cytotoxic T cell degranulation [51], or to vesicular IL-8 secretion by airway epithelial cells [52]; (ii) elevated Ca^{2+} levels near the plasma membrane could facilitate vesicular membrane fusion [53]; (iii) other signaling pathways might be affected by Ca^{2+} even though we did not observe any impact of vitamin C on CAMKII and CREB. It is known that Ca^{2+} fluctuations are crucial in the endoplasmic reticulum for Ca^{2+}-binding chaperones such as BiP, CyPB, and calreticulin to bind and release collagen, as Cabral et al. revealed by studying the null mutations of the cation channel TRIC-B encoding gene TMEM38B in osteogenesis imperfecta [54]. Theoretically, the excess intracellular [Ca^{2+}] generated by vitamin C-elicited Ca^{2+} influx could be transported into the endoplasmic reticulum via pumps, where elevated [Ca^{2+}] would increase chaperon activity. Ultimately, this could stabilize collagen assembly and induce post-translational modifications that would culminate in enhanced collagen release. However, these theories remain to be verified experimentally.

Assessing the role of ORAI1 in the vitamin C-induced Ca^{2+} influx, we found that the influx into PS-1 cells and murine PSCs is blockable by Synta-66. However, si*ORAI1* application left the Ca^{2+} influx unaffected, indicating that ORAI1 is not the primary ion channel in charge. Even though Synta-66 is selective for Ca^{2+}-release activated Ca^{2+} (CRAC) channel inhibition over inhibition of $K_V1.3$, hERG, TRPM4, or TRPM7 channels [55], we postulate that Synta-66 has yet unknown off-target inhibitory effects on other Ca^{2+}-permeable channels. Alternatively, the partial reduction in Ca^{2+} influx observed with Synta-66 could be due to a secondary mechanism where the initial Ca^{2+}entry, potentially through a different membrane channel, triggers Ca^{2+} release from intracellular stores. This release might activate store-operated Ca^{2+} entry, involving ORAI1 to a lesser extent and explaining the partial inhibition observed with Synta-66 but not with siRNA-mediated *ORAI1* knockdown.

Based on the result that NIH-3T3 cells do not respond to vitamin C with Ca^{2+} influx, it is likely that vitamin C-induced Ca^{2+} influx is not present or is overridden by other mechanisms in these cells. It is known that Synta-66 inhibits ORAI1, activates ORAI2, and does not affect ORAI3 [45]. Thus, the finding that vitamin C together with Synta-66 induces a marked Ca^{2+} entry in NIH-3T3 might be due to Synta-66 activating Orai2 [56]. Given that vitamin C is an important metabolite in the human body, we believe that further mechanistic characterization of the vitamin C-induced Ca^{2+}entry is warranted in more specialized model systems.

We revealed that ORAI1 inhibition, both with si*ORAI1* and Synta-66, resulted in diminished collagen release from PS-1 cells. When applying Synta-66 to murine PSCs we observed the same phenomenon. However, the collagen release from the fibroblast cell line NIH-3T3 was not affected by Synta-66. These findings indicate that ORAI1-regulated collagen release may not be a general phenomenon applicable to all

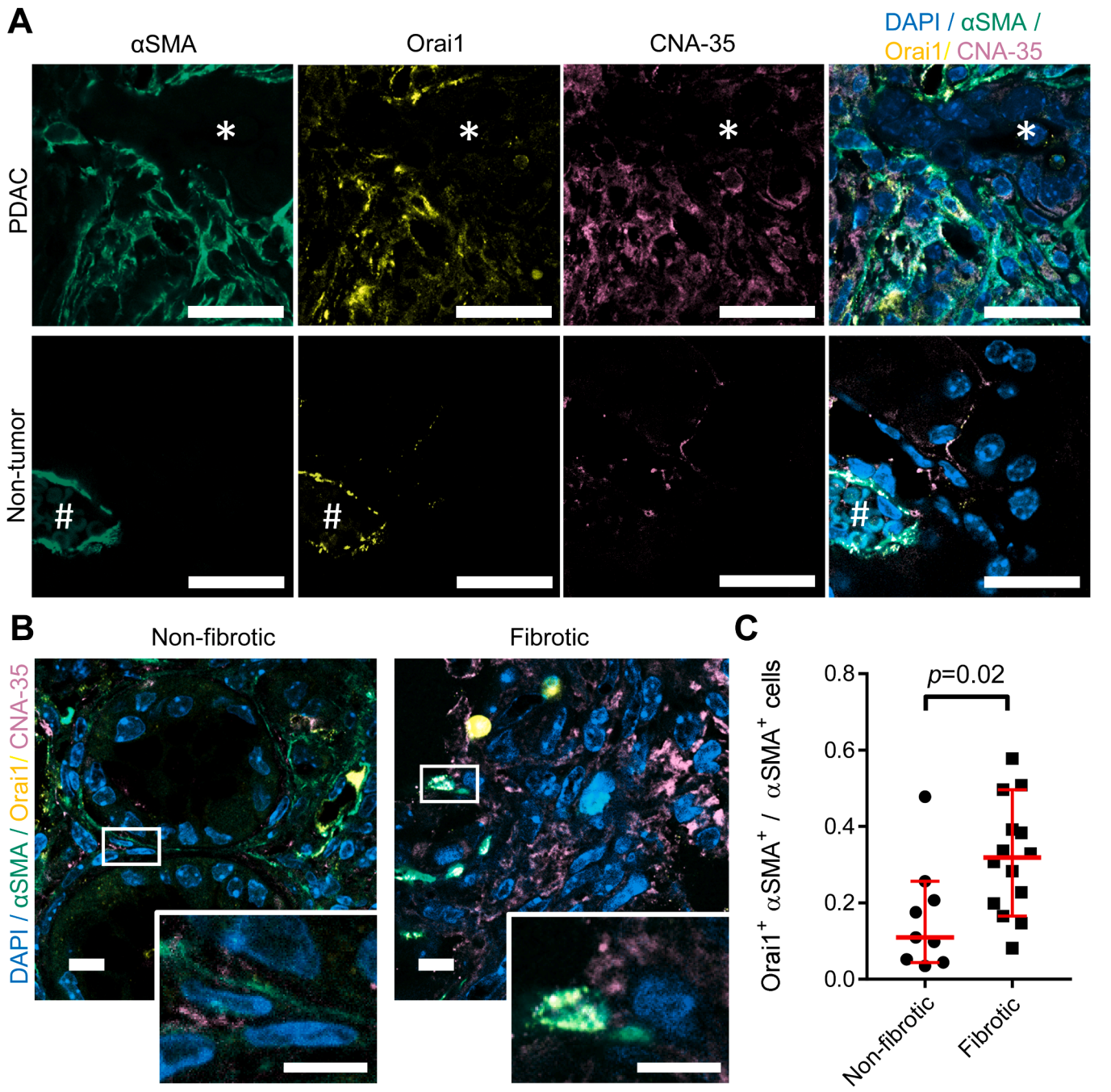

Fig. 6. Orai1 is expressed in the fibrotic PDAC tissue.
(A) Representative immunohistochemistry images of PDAC tissue and neighboring non-tumorous tissue ($N = 4$) stained for the CAF marker αSMA (cyan), the Ca^{2+} channel Orai1 (yellow), the collagen-binding CNA-35-tdTomato (magenta) and DAPI (blue). * marks a nest of tumorous ductal cells, # marks a blood vessel, scale bar = 20 μm. (B) Representative immunohistochemistry images ($N = 4$) stained for markers detailed in (A) depict non-fibrotic versus fibrotic tumor nodes that differ in CNA-35-tdTomato staining intensity, scale bar = 20 μm. Inset, magnified from the white rectangle, highlights $αSMA^+$ CAFs in the tumor lining with differential Orai1 staining pattern, scale bar = 10 μm. (C) Scatter plot depicts the ratio of $Orai1^+$ $αSMA^+$ cells compared to all $αSMA^+$ cells with each data point representing an individual tumor node ($N = 4$ mice with $n_{Non\text{-}fibrotic} = 9$, $n_{Fibrotic} = 14$ tumor nodes). Data in (C) are displayed as mean±SEM with statistical comparison using Student's *t*-test.

fibroblasts. Instead, it might be specific to stellate cells. This could be attributed to different sets of ion channels and the expression of different Orai isoforms which requires further investigations.

We further proceeded to assess the pathophysiological role of ORAI1 in fibrosis. We detected Orai1 primarily in $αSMA^+$ CAFs, especially in fibrotic tumor nodes. We, therefore, want to emphasize the role of Orai1 within the stromal compartment, particularly in CAFs and PSCs. A recent study showed that the PSC cell line PS-1 expresses ORAI1 channels: ORAI1 in PS-1 cells promotes AKT signaling, cell proliferation, and TGF-β1 secretion [26]. Considering our results, the involvement of ORAI1 in TGF-β1 secretion is likely a positive feedback cycle that further augments PS-1-mediated collagen deposition.

As vitamin C has been intensively studied in fibrosis since its original description almost 100 years ago (in 1928, Albert Szent-Györgyi isolated this substance from adrenal glands), we were initially surprised that its link to Ca^{2+} entry in myofibroblasts is obscure. For cancer, it is not

entirely novel that vitamin C can modulate cellular Ca^{2+} homeostasis. It can induce Ca^{2+} influx, e.g., into retinoblastoma and laryngeal carcinoma cells [24,25]. Moreover, pharmacologic vitamin C treatment (4 g ascorbate/kg body weight/day) inhibits the growth of pancreatic tumor xenografts and displays synergistic cytotoxic effects when combined with gemcitabine in pancreatic cancer [57,58]. However, earlier *in vitro* studies used excessively high concentrations of 10–20 mM, presumably heavily altering the redox homeostasis and/or impacting cell volume homeostasis [59,60]. In contrast, we used vitamin C in an approximately 35 times lower, physiologically relevant concentration which already promotes collagen deposition and release. Reflecting on our data, vitamin C would act profibrotic in pancreatic cancer. The profibrotic effects of vitamin C treatment could be beneficial, especially at the early stages of the PDAC, by further isolating cancer cells. As a complete lack of fibrosis is detrimental, and excessive fibrosis may also worsen late PDAC prognosis, partial inhibition of PDAC fibrosis by impairing ORAI1 seems therapeutically plausible. The clinical applicability of Synta-66, however, may be limited because of its high IC_{50} value. Alternatively, a drug similar to Synta-66, namely CM4620 can be considered in the clinical setting, as it is currently undergoing Phase II clinical trials to treat pneumonia in COVID-19 patients and acute pancreatitis [61,62]. Combined with the fact that ORAI1 promotes PSC proliferation [26], pharmacologic ORAI1 inhibition would stop the positive feedback cycle leading to PDAC desmoplasia.

Methods

Animal experiments

20-week-old untreated, tumor-bearing KPfC-mice, harboring heterozygous loss of p53 and conditionally expressed mutant K-Ras (K-Ras^{G12D}) from the endogenous locus in the pancreas (*Kras*$^{wt/LSL–G12D}$ *Tp53*$^{fl/+}$ *Pdx1-Cre*$^{+}$) [63–65], were sacrificed to obtain PDAC tissue slices for immunohistochemistry experiments. For obtaining primary murine PSCs, heterozygous animals that harbor heterozygous loss of p53 but express wildtype K-Ras (*Kras*$^{wt/wt}$ *Tp53*$^{fl/+}$ *Pdx1-Cre*$^{+}$) were sacrificed. Mice were housed in individually vented cages (IVC) containing nesting material. Constant ambient temperature (22 °C ± 2 °C), constant humidity (55 % ± 10 %), and a 12-hour light/12-hour dark cycle were provided. All animal experiments were approved by the local authorities (LANUV).

Murine PSC isolation

PSCs from the murine pancreas were isolated as previously described [37–39,43]. Briefly, whole murine pancreata were removed, dissected, and enzymatically digested using 0.1 % collagenase P (Sigma-Aldrich, Merck KGaA) at 37 °C for 25 min in an orbital shaker. Next, digested pancreatic tissue was centrifuged at 200 g at RT for 5 min, followed by resuspending the homogenized tissue in Dulbecco's Modified Eagle's Medium/Ham's Nutrient Mixture F12 cell culture medium (DMEM/Ham F12 1:1, supplemented with 10 % FCS and 1 % penicillin/streptomycin; Sigma-Aldrich). Then, tissue homogenizate was seeded onto FCS-coated tissue culture dishes. PSCs were allowed to adhere for 2 h, followed by a vigorous washing step that removed all nonadherent cells. This resulted in a homogeneous PSC culture, which was cultured for 120 h, and then used for the subsequent experiments.

Cell lines

The telomerase reverse transcriptase (TERT)-immortalized human pancreatic stellate cell line PS-1 [30] was used for our mechanistic studies and to produce cell-derived matrix for various downstream assays. PS-1 cells were cultured in DMEM/Ham-F12 medium supplemented with 10 % FCS and 1 % penicillin-streptomycin. The human pancreatic epithelioid carcinoma-derived Panc-1 cell line and the murine embryonic fibroblast cell line NIH-3T3 were cultured in Dulbecco's Modified Eagle's Medium (high glucose) supplemented with 1 % glutamine and 10 % FCS. All cells were kept in an incubator at 37 °C and 5 % CO_2, then washed, trypsinized, and counted before applying them for downstream assays.

ORAI1 knockdown

Silencing of ORAI1 gene expression was performed as described previously [26]. Briefly, PS-1 cells, reaching a confluence of approximately 60 %, were transfected with either *ORAI1* siRNA (ON-TARGETplus siRNA, Dharmacon) or scrambled siRNA (AllStars Negative Control siRNA, Qiagen) using Lipofectamine RNAiMAX Reagent (Invitrogen), following manufacturer's protocol. For confirming gene silencing, RT-qPCR was performed 48 h after silencing with the PowerUp™SYBR®Green Mastermix (Thermo Fisher) using a QuantStudio™ 3 cycler (Thermo Fisher) and analyzed by the QuantStudio™ Design & Analysis Software (Thermo Fisher). For RT-qPCR quantification, *ORAI1, ORAI2,* and *ORAI3* gene expression were normalized to the mean expression of the housekeeper genes *GAPDH*. Primers for all genes tested were established previously [66]: *GAPDH* (NM_002046), FW: ACGACCCCTTCATTGACCTCA, Rev: TTTGGCTCCACCCTTCAAGTG; *ORAI1* (NM_032790), FW: ACCTCGGCTCTGCTCTCC, Rev: GATCATGAGCGCAAACAGG; *ORAI2* (NM_032831), FW: TACCTGAGCAGGGCCAAG, Rev: TGGCCACCATGGCAAAG; *ORAI3* (NM_152,288), FW: ACGTCTGCCTTGCTCTCG, Rev: GAGTGCAAAGAGGTGCACAG.

Cell-derived matrix production

This study aimed to establish an assay for pancreatic stellate cell-derived matrix production *in vitro*. A protocol by Kaukonen et al. served as a basis [36] including three key steps: cell seeding and stimulation, matrix deposition, and matrix extraction — these steps in the protocol needed to be adapted to PSCs. We found 15,000 PS-1 cells as optimal to be seeded in each well of a 96 well/plate. Then, PS-1 cells were cultured in DMEM/Ham-F12 (pH 7.4, 10 % FBS) for 4 days until reaching confluency. Then, the medium was changed to DMEM/Ham-F12 medium (pH 7.4, 0.5 % FBS) supplemented with vitamin C (50 μg/ml, 284 μM; Sigma-Aldrich) ± TGF-β1 (10 ng/ml; Peprotech) to stimulate matrix production. Vitamin C was replaced daily due to its short half-life [67]. This was done by replacing half the volume of the medium with fresh medium containing the doubled concentration of vitamin C as proposed by other studies before [68]. Vitamin C was freshly dissolved daily and was filtered with sterile filters (0.22 μm pore size) to eliminate unsolved crystals. In samples treated with 10 μM Synta-66 (AK Scientific), Synta-66 was also replaced daily to maintain the 10 μM concentration. In respective controls, 0.1 % DMSO was added as a vehicle.

Cell-derived matrix decellularization

Sirius Red is not highly specific for ECM proteins, as it also detects basic amino acids of other proteins [33]. Methodically, this means that matrices need to be decellularized, otherwise the signals of cellular proteins overshadow the matrix signals. For COL1A1 and CNA35-tdTomato, this step is not necessary in native samples as cellular protein signal is negligible. However, matrices were similarly decellularized under each condition to keep the results comparable with Sirius Red when indicated.

For matrix extraction, the matrices were decellularized as follows. First, the medium was aspirated. Afterwards, cells were washed with PBS. In a next step, the extraction solution (PBS with 0.1 % Triton-X and 2 % NH_4OH) was added for around 60 s while checking the progress of cell removal under a phase contrast microscope. Next, the extraction solution was carefully removed, and the remaining matrix was washed with PBS. Remaining DNA was removed by incubating the matrix with

DNaseI (Invitrogen) in a concentration of 10 μg/ml in PBS supplemented with 5 mM $MgCl_2$. DNase was incubated for 60 min in a warming cabinet at 37 °C.

CNA-35-tdTomato production and purification

CNA35-tdTomato staining solution was extracted on a large scale from E. coli BL21(DE3) competent bacteria (Novogen) transformed with the pET28a-tdTomato-CNA35 plasmid (pET28a-tdTomato-CNA35 was a gift from Maarten Merkx (Addgene plasmid #61,606; RRID: Addgene_61,606) based on the original protocol by Aper et al. [46]. For culturing the E. coli, LB medium was produced according to the manufacturer's instructions (BD Bioscience) and was supplemented with kanamycin in a final concentration of 10 μg/ml. Bacterial growth was arrested at an optical density of 0.6 at 600 nm, measured with a photometer (Eppendorf BioPhotometer 6131). Next, CNA35-tdTomato protein expression was induced by adding isopropyl-β -d-1-thio-galactopyrano-side (IPTG, AppliChem PanReac) at a final concentration of 1 mM. IPTG-based protein induction was conducted in a bacterial incubator for 20 h at 37 °C with continuous shaking at 220 rpm. Next, bacterial cells were lyzed, then centrifuged in an ultracentrifuge (Avanti JXN-26, Beckman Coulter) at 4000 g and 4 °C for 20 min. Bacterial pellet was washed twice in a solution containing 50 mM NaPi and 300 mM NaCl, pH 7, followed by centrifugation steps at 4000 g and 4 °C for 20 min. Lysozyme (10 mg/ml) and protease inhibitor cocktail III (Calbiochem) were added to the samples and incubated on ice for 30 min on an orbital shaker for another 10 min. Afterwards, 0.1 % Triton X-100 (Sigma Aldrich), DNase I (1 mg/ml) (Invitrogen) and RNase A (1 mg/ml) (AppliChem PanReac) were added in a $MgCl_2$ solution (1 M), followed by sonication on ice for 3 × 60 s with 60 s breaks between each cycle. After that, cells were mechanically lyzed with a French press. The lysates were centrifuged at 4 °C and 12,500 g for 45 min.

Resulting protein-containing supernatants were purified using nickel-nitrilotriacetic acid (Ni-NTA) agarose beads (Qiagen), according to the manufacturer's instructions. Briefly, beads were washed, then mixed with the protein-containing bacterial supernatant on ice on an orbital shaker for 60 min, allowing the 6xHis-tag of CNA35-tdTomato proteins to attach to the Ni-NTA Agarose beads. After centrifugation and washing, CNA35-tdTomato-attached bead pellets were loaded into filter columns (Cytiva). After multiple washing steps, 250 mM imidazole was added to elute the 6xHis-tagged CNA35-tdTomato proteins bound to the beads. The eluate was collected and concentrated using Amicon Ultra 0.5 ml 10k diafiltration filters, washed, then the filters were turned upside down and centrifuged for 2 min at 1000 g and 4 °C to collect the concentrated CNA35-tdTomato proteins. As a last step, the protein lysates were kept at 37 °C overnight to promote fluorescent protein maturation.

With the method described above, we obtained high quantities of purified CNA35-tdTomato protein solution and determined its concentration (1.037 mg/ml) using a BCA Protein Assay Kit (Pierce). CNA35-tdTomato protein solution was aliquoted and kept for long-term storage at −70 °C.

Immunohistochemistry

IHC from KPfC tissue slices was performed as previously described [38]. Briefly, pancreata were fixed in 4 % paraformaldehyde, embedded in paraffin, and then cut into 6 μm sections with a RM2125 microtome (Leica). Afterward, sections were deparaffinized with xylene, rehydrated in a stepwise manner. Antigen retrieval was performed using 10 mM sodium citrate buffer (pH 6.0), followed by blocking with 1 % BSA-containing PBS (Sigma-Aldrich) for 1 h Slides were stained with primary anti-ORAI1 antibody (75,522, RRID: AB_11,007,920, 1:100, Novus Biologicals) in a humidified chamber at 4 °C overnight. After washing 3 times in PBS, secondary antibody labeling was performed using donkey anti–mouse Alexa Fluor 647 (A-31,571, RRID: AB_162,542, 1:1000, Thermo Fisher) at RT for 2 h After washing 3 times in PBS, slices were labeled with Alexa Fluor 488–conjugated mouse anti-αSMA (53–9760–82, RRID: AB_476,701, 1:600, Thermo Fisher) and CNA-35-tdTomato (1:200) at RT for 2 h Slides were mounted in DAKO mounting medium (Agilent) with 0.001 % DAPI (Sigma-Aldrich, Merck KGaA) and covered with coverslips. Confocal microscopy was performed on a Nikon Ti-2 setup (Nikon) in the NIS Elements AR software using excitation wavelengths of 405 nm, 488 nm, 514 nm, and 633 nm, with a 630× total magnification.

IHC image analysis was performed in the QuPath software (RRID: SCR_018257) [69]. First, cells were detected based on DAPI fluorescence intensity using the built-in cell detection algorithm. Then, a pixel classifier was trained to detect αSMA and ORAI1-positive cells. The classifier output was compared to manual classification, and training was stopped when the automatic classification was at least as accurate as the manual classification. To differentiate between fibrotic and non-fibrotic tumor nodes, individual tumor nodes were manually segmented and then binned depending on their CNA-35-tdTomato mean fluorescence intensity.

Visualization of cell-derived matrix secretion and accumulation

Cell-derived ECM was visualized by Sirius Red, COL1A2, and CNA35-tdTomato stainings. For Sirius Red detection, cell-derived matrices were decellularized, washed with PBS, then stained with Picrosirius Red Stain (F3BA, solution B, Roche) for 20 min. Subsequently, matrices were washed four times with 0.1 M HCl. Finally, absolute ethanol was added to prevent matrix shrinkage.

For COL1A2 immunostaining, cell-derived matrices were decellularized, then washed twice with PBS. Afterwards, samples were blocked with 1 % BSA in PBS for 30 min. Next, samples were incubated with primary antibody against COL1A2 (14,695–1-AP, RRID: AB_2,082,037, 1:500, Proteintech) in 1 % BSA in PBS for 2 h at 4 °C. Dishes were washed three times with PBS, followed by incubation with the secondary antibody Alexa Fluor™ 488 goat anti-rabbit (A-11,008, RRID: AB_143,165, 1:1000, Invitrogen) in 1 % BSA-PBS at RT for 20 min. Finally, samples were washed three times with PBS.

CNA35-tdTomato stainings were performed following the original description [46]. When compared to Sirius Red, matrices were first decellularized. Otherwise, matrices were washed with PBS. Then, matrices were incubated with CNA35-tdTomato (1:200) in PBS at room temperature for 2 h Afterwards, samples were washed three times with PBS.

The sensitivity and specificity of CNA35-tdTomato allowed for intracellular and extracellular collagen staining at a single-cell level. 5000 PS-1 cells were seeded into glass-bottom dishes in DMEM/Ham-F12 medium (10 % FBS). Non-confluent PS-1 cells were allowed to adhere for 24 h Then, cells were treated with vitamin C (284 μM) and TGF-β1 (10 ng/ml) in DMEM/Ham-F12 medium (0.5 % FBS) for another 24 h For a combined intracellular and extracellular collagen staining (data displayed in Figs. 2 and 4), cells and matrices were fixed with 4 °C methanol for 5 min, washed three times with PBS, and then stained with CNA-35-tdTomato (1:200) in PBS for 2 h in the dark at room temperature. For live cell staining (data displayed in Fig. 6), dishes were washed with PBS and stained at RT with CNA35-tdTomato (1:250) in PBS for 30 min, then washed three times with PBS.

Images were acquired with the 63x oil immersion objective of a Zeiss Axio Observer D1 microscope (Zeiss) or Nikon Ti-2 confocal microscope (Nikon). Sirius Red was either imaged with brightfield microscopy or fluorescence microscopy as Sirius Red displays an intrinsic fluorescence when excited at 561 nm wavelength [70]. COL1A2 was detected upon excitation with 488 nm, and CNA35-tdTomato with 514 nm.

Cell-derived matrix quantification

Cell-derived ECM was quantified by Sirius Red as well as using

CNA35-tdTomato in a 96-well-plate based assay. For quantitative Sirius Red staining, matrices were decellularized, washed once with PBS, and stained with Picrosirius Red Stain (F3BA, solution B, Roche) for 20 min. Next, matrices were washed four times with 0.1 M HCl. To quantify matrix amounts, absorbance measurements were performed with a microplate reader (ThermoMax, Molecular Devices) at 546 nm. Measured intensities were blank-corrected and subtracted by the reference wavelength of 650 nm, which is independent of Sirius Red absorbance.

Because of the specificity of CNA35-tdTomato for collagens compared to other proteins [47], staining was performed either on decellularized cell-derived matrix (Fig. 2), or on cell-derived matrices still containing live cells (Fig. 6). CNA35-tdTomato staining solution (1:50) in PBS was incubated for 3 h at room temperature in the dark. In cell-derived matrices containing live cells, incubation time was shortened to 20 min to minimize dye internalization. The staining solution was removed, and samples were washed three times with PBS. For matrix quantification, fluorescence intensities were measured with a fluorescence plate reader (Fluoroskan II). CNA35-tdTomato was excited at 544 nm and emission was detected at 590 nm. Measured intensities were then blank corrected.

To assess the detection threshold and assay linearity of Sirius Red for PS-1 cell-derived matrix quantification, rat tail collagen standards were produced and stained to plot a standard curve. 1 mg/ml Rat tail collagen type I (Corning) in PBS was incubated with Sirius Red on ice for 20 min. Afterwards, the mixture was centrifuged at 5000 g and 4 °C for 10 min. The supernatant was discarded, and the pellet was washed four times with 0.1 M HCl. Next, the pellet was resuspended in PBS. From there, a serial dilution (1:2 with PBS) was performed to obtain collagen concentrations of 0.5 mg/ml, 0.25 mg/ml, 0.125 mg/ml, 0.063 mg/ml, 0.031 mg/ml and 0.016 mg/ml. 100 µl stained collagen of each concentration were added into 96-well plates. Absorbance measurements were performed as described above.

To determine whether the Sirius Red and CNA-35-based matrix production assays are suitable for high-throughput screening, we applied the Z' quality metric [34]. The Z' factor is derived from the standard deviations (SD) and means ($\bar{x}$) of positive (p) and negative (n) control samples as:

$$Z' \text{ factor} = 1 - \frac{3\left(SD_p + SD_n\right)}{\left|\bar{x}_p + \bar{x}_n\right|}$$

Absorbance and fluorescence readouts from PS-1 cells stimulated with medium were used as the negative control, and readouts from cells stimulated with VitC+TGF-β1 were used as the positive control. An ideal assay would have a Z'=1, and negative values imply that the variance between groups is not high enough to provide reliable readouts in a high-throughput assay [34].

Cell viability assay

Cell viability was assessed with the CellTiterGlo assay, as performed previously [71]. Briefly, after detecting CNA35-tdTomato fluorescence intensities with the plate reader, wells were supplemented with CellTiterGlo solution. After orbital shaking with 220 g at RT for 20 min, well luminescence was detected and blank-corrected with a luminescent plate reader (GloMax® Discover, Promega).

Cell migration assay

Panc-1 cells were seeded on different substrates onto T-12.5 cell culture flasks. Flasks were either uncoated; coated with a reconstituted ECM containing 40 µg/mL laminin (Sigma-Aldrich, Merck KGaA), 40 µg/mL fibronectin (Sigma-Aldrich), 800 µg/mL collagen I (Corning), 12 µg/mL collagen III (Corning), and 5.4 µg/mL collagen IV (BD Biosciences) as published previously [37–39,72], or coated with decellularized cell-derived matrix, as detailed above. 70 000 Panc-1 cells were seeded into each flask in a suspension with DMEM. After cell seeding, flasks were put back to the incubator overnight to let the cells adhere to the underlying substrates. Before removing the flasks from the incubator on the next day, caps were tightly closed to keep a constant 5 % CO_2. The flasks were transferred to chambers heated to 37 °C for live cell imaging. Cell migration was recorded with CMOS cameras (MikroCam SP 3.1, Bresser) and Axiovert 40C inverted phase contrast microscopes (Zeiss) for 24 h in 15 min intervals.

Cell migration experiments were analyzed with the Amira–Avizo Software Version 2019.2 (Thermo Fisher). The contours of migrating Panc-1 cells were segmented manually. The x- and y-coordinates of the geometric cell centers were tracked over time to deduce trajectories. Quantitative parameters were determined to characterize the migratory behavior: velocity (µm/min), translocation (µm), circularity, and persistence. Velocity is derived by covered distance per time interval, whereas translocation indicates the net distance between the starting and end points. Cell persistence is determined by the quotient of total path length covered during the course of the experiment (24 h) and translocation. Accordingly, persistence has arbitrary units that vary between 0 and 1, where higher values reflect a more persistent migration. The circularity is calculated by using the formula $Circularity = \frac{4\times\pi\times area}{perimeter^2}$. If cells are perfectly circular, the circularity value is '1'. In contrast, circularity values approach '0' for more branched cells.

Cell coordinates (x, y) were used to derive the vectors between successive positions of the cell centroids. Angles between two consecutive vectors (direction at t_n vs. direction at t_{n+1}) are defined as the turning angles. Turning angles are calculated with the formula: $\alpha = cos^{-1}\left(\frac{\vec{u}\times\vec{v}}{|\vec{u}|\times|\vec{v}|}\right)$, where $\vec{u}$ and $\vec{v}$ represent consecutive vectors. $\vec{u}\times\vec{v}$ is the scalar product, $|\vec{u}|\times|\vec{v}|$ is the product of the vectors' magnitudes. A positive or negative α indicates a positive or negative vector along the y axis, respectively. Accordingly, a turning angle of 0° means a continuous, undisrupted vector, whereas ±180° means that the vector direction is reversed, i.e., the cell turns around.

Western blot and mass spectroscopy

To obtain sufficient quantity of cell-derived matrix for Western blot and mass spectroscopy, PS-1 cells were cultured in 10 cm tissue culture dishes according to protocols described above. After decellularization, cell-derived matrix was brought into solution as follows. First, the matrix deposited into tissue culture dishes was mechanically comminuted, i.e., chopped using a scalpel. Then, cell-derived matrix was solubilized with a buffer composed of 8 M urea, 2 % SDS and 100 mM TRIS. PS-1 cell lysates were obtained using a radioimmunoprecipitation (RIPA) buffer as described previously [39].

Gel electrophoresis was performed on 7.5 % PAGE gels and gels were applied for Coomassie staining and COL1A2 Western Blotting. To increase the protein amounts for the mass spectroscopy analysis, three samples were pooled. Mass spectroscopy was performed by Prof. Simone König's group (IZKF Core Unit Proteomics, Münster). The samples were reduced, alkylated and tryptically digested. The analysis was performed by applying label-free liquid chromatography mass spectrometry (data-independent analysis mode, LC-MSE, Synapt G2 Si, Waters Corp.). The evaluation was performed with Progenesis (Waters).

Spectrofluorometry

To record Fura-2 excitation spectra in the presence or absence of vitamin C, Fura-2 was used (Fura-2 potassium salt, Sigma-Aldrich). Measurements were performed in cuvettes using a FP-8300 fluorescence spectrometer. Fura-2 was dissolved in Ringer's solution with two different Ca^{2+} concentrations: 1.2 mM Ca^{2+} and Ca^{2+}-free EGTA-supplemented Ringer's solution (0 mM Ca^{2+}). Excitation spectra were

recorded in both solutions, in each case without vitamin C as well as in the presence of 10 μM, 284 μM, or 1 mM vitamin C.

Ca^{2+} measurements

Ca^{2+}imaging was conducted with the ratiometric Ca^{2+} indicator Fura-2, as done previously [37,39,66,71]. After cells had adhered overnight onto glass-bottom dishes (VWR), cells were loaded with 3 μM Fura-2AM dissolved in HEPES-buffered RPMI-1640 medium for 30 min at 37 °C. After loading, PS-1 cells were washed with prewarmed HEPES-buffered Ringer's solution (140 mM NaCl, 5.4 mM KCl, 1.2 mM $CaCl_2$, 0.8 mM $MgCl_2$, 5.5 mM glucose, 10 mM HEPES, pH 7.4). Then, cells were placed inside the 37 °C-temperated heating chamber of the imaging setup consisting of an inverted Axiovert 40 C microscope connected to a MikroCam SP 3.1, a high-speed shutter and a polychromator.

During the experiments, cells were steadily superfused with prewarmed solutions. After a superfusion with Ringer's solution for 200 s, the inflow was changed to Ringer's solution supplemented with vitamin C in the following concentrations: 10 μM, 100 μM, 284 μM and 1 mM. Fura-2 was alternately excited at 340 nm and 380 nm, and emission intensities were captured at 510 nm in intervals of 10 s using the VisiView software (Visitron Systems). Average cellular fluorescence intensities were background-corrected. Subsequently, F_{340}/F_{380} ratios were determined. Increasing F_{340}/F_{380} ratios reflect increasing intracellular Ca^{2+}.

To assess whether Ca^{2+} is released from intracellular stores, cells were incubated in Ca^{2+}-free EGTA-supplemented Ringer's solution (140 mM NaCl, 5.4 mM KCl, 0.8 mM $MgCl_2$, 5.5 mM glucose, 10 mM HEPES, 1 mM EGTA, pH7.4), followed by adding vitamin C dissolved in Ca^{2+}-free EGTA-supplemented Ringer's solution to reach the final concentration of 284 μM. Lastly, we changed the superfusion solution to Ca^{2+}-containing Ringer's solution supplemented with 284 μM vitamin C.

For the Mn^{2+} quench experiments, Fura-2 was excited at its isosbestic wavelength of 357 nm where the signal is independent of the intracellular Ca^{2+} concentration [37], and emission intensities were recorded at 510 nm. Mn^{2+}binds Fura-2 with a higher affinity than Ca^{2+} and quenches its fluorescence [73]. Thus, detected changes in the fluorescence activity of Fura-2 are due to Mn^{2+}-dependent quenching effects, i.e. the level of negative steepness of the recorded curves is a measure of Ca^{2+}influx. During the measurements, Fura-2AM-loaded-cells were initially superfused with Ringer's solution. To ensure proper binding of Synta66 to ORAI1 channels, PS-1 cells were preincubated with 10 μM Synta-66, or in case of control, with 0.1 % DMSO. Then, cells were superfused with Ca^{2+}-free, 1 mM Mn^{2+}-supplemented Ringer's solution with 284 μM vitamin C, 10 μM Synta-66 or 0.1 % DMSO. When indicated, the cells were pretreated with vitamin C and TGF-β1 for 24 h prior to the experiment. Mn^{2+} entry rates were calculated from the negative slopes upon superfusion with Ca^{2+}-free, 1 mM Mn^{2+}-supplemented Ringer's solution, which were subtracted by the respective slopes of the curves before adding Mn2+-containing solutions to compensate for potential photobleaching effects. Then, Mn^{2+} entry rates were indicated as Mn^{2+} influx per minute ($\Delta F/F_0$/min).

Statistics

Statistical analyses and graphics generation were performed using Excel and GraphPad Prism, respectively. "N" indicates the number of independent test series, whereas "n" indicates the number of datapoints, e. g. the number of analyzed single cells or the number of wells in 96-well plates experiments. Experiments were performed with $N \geq 3$. The Shapiro-Wilk was applied to test for normal distribution. In the case of normally distributed data, the data is presented as mean ± SEM (standard error of the mean). When comparing two groups with normally distributed data, Student's *t*-test was applied as a significance test. Comparison of more than two groups was performed with ordinary one-way ANOVA (analysis of variance) with Tukey's post-hoc test. In the case of not normally distributed data, the data is presented as median ± 95 % confidence interval, and multiple comparisons were performed using the Kruskal-Wallis test with Dunn's post-hoc test. Statistical testing is based on a significance level of $\alpha = 0.05$ (two-tailed).

Declaration of competing interest

The research was conducted in the absence of any commercial or financial competing interests.

Acknowledgements

We are thankful to Prof. König at the Core Facility Proteomics of the University of Münster for her help with mass spectroscopy, and to Dr. Tiffany Paulisch (Institute of Organic Chemistry, University of Münster) for help with spectrofluorometry. AS was funded by IZKF Münster (Schw2-020-18), Deutsche Forschungsgemeinschaft (DFG; SCHW407/22-1 & 25–1) and the EU (Horizon 2020 Marie Skłodowska-Curie grant pHioniC, No 813834). AO was funded by the DFG (OE531/4-1). RS was supported by the MedK fellowship. ZP acknowledges funding by the DFG (PE 3917/2-1).

Supplementary materials

Supplementary material associated with this article can be found, in the online version, at doi:10.1016/j.matbio.2024.12.004.

Data availability

This study includes no data deposited in external repositories. All raw data and further information and analytic methods that support the findings are available upon request from the corresponding author.

References

[1] R.L. Siegel, A.N. Giaquinto, A. Jemal, Cancer statistics, 2024, CA Cancer J. Clin. 74 (2024) 12–49, https://doi.org/10.3322/caac.21820.
[2] D. Wang, Y. Li, H. Ge, T. Ghadban, M. Reeh, C. Güngör, The extracellular matrix: a key accomplice of cancer stem cell migration, metastasis formation, and drug resistance in PDAC, Cancers. (Basel) 14 (2022) 1–22, https://doi.org/10.3390/cancers14163998.
[3] R.R. Bynigeri, A. Jakkampudi, R. Jangala, C. Subramanyam, M. Sasikala, G.V. Rao, D.N. Reddy, R. Talukdar, R.R. Bynigeri, A. Jakkampudi, R. Jangala, Pancreatic stellate cell: pandora ' s box for pancreatic disease biology, 23 (2017) 382–405. https://doi.org/10.3748/wjg.v23.i3.382.
[4] M. Erkan, C. Reiser-Erkan, C.W. Michalski, B. Kong, I. Esposito, H. Friess, J. Kleeff, The Impact of the Activated Stroma on Pancreatic Ductal Adenocarcinoma Biology and Therapy Resistance, Curr. Mol. Med. 12 (2012), https://doi.org/10.2174/156652412799218921.
[5] C.J. Whatcott, C.H. Diep, P. Jiang, A. Watanabe, J. Lobello, C. Sima, G. Hostetter, H.M. Shepard, D.D. Von Hoff, H. Han, Desmoplasia in Primary Tumors and Metastatic Lesions of Pancreatic Cancer, (n.d.) 3561–3568. https://doi.org/10.1158/1078-0432.CCR-14-1051.
[6] C. Tian, K.R. Clauser, D. Öhlund, S. Rickelt, Y. Huang, M. Gupta, D.R. Mani, S. A. Carr, D.A. Tuveson, R.O. Hynes, Proteomic analyses of ECM during pancreatic ductal adenocarcinoma progression reveal different contributions by tumor and stromal cells, Proc. Natl. Acad. Sci. u S. a 116 (2019) 19609–19618, https://doi.org/10.1073/pnas.1908626116.
[7] V.M. Perez, J.F. Kearney, J.J. Yeh, The PDAC extracellular matrix: a review of the ECM protein composition, tumor cell interaction, and therapeutic strategies, Front. Oncol. 11 (2021) 1–10, https://doi.org/10.3389/fonc.2021.751311.
[8] M.B. Lankadasari, P. Mukhopadhyay, S. Mohammed, K.B. Harikumar, TAMing pancreatic cancer: combat with a double edged sword, Mol. Cancer 18 (2019) 1–13, https://doi.org/10.1186/s12943-019-0966-6.
[9] Y. Sunami, V. Böker, J. Kleeff, Targeting and Reprograming Cancer-Associated Fibroblasts and the Tumor Microenvironment in Pancreatic Cancer, (2021) 1–14.
[10] B.C. Özdemir, T. Pentcheva-Hoang, J.L. Carstens, X. Zheng, C.-C. Wu, T. R. Simpson, H. Laklai, H. Sugimoto, C. Kahlert, S.V. Novitskiy, A. De Jesus-Acosta, P. Sharma, P. Heidari, U. Mahmood, L. Chin, H.L. Moses, V.M. Weaver, A. Maitra, J.P. Allison, V.S. LeBleu, R. Kalluri, Depletion of carcinoma-associated fibroblasts and fibrosis induces immunosuppression and accelerates pancreas cancer with reduced survival, Cancer Cell 25 (2014) 719–734, https://doi.org/10.1016/j.ccr.2014.04.005.
[11] Y. Chen, J. Kim, S. Yang, H. Wang, C.J. Wu, H. Sugimoto, V.S. LeBleu, R. Kalluri, Type I collagen deletion in αSMA^{+} myofibroblasts augments immune suppression

and accelerates progression of pancreatic cancer, Cancer Cell 39 (2021) 548–565, https://doi.org/10.1016/j.ccell.2021.02.007, e6.
[12] A.D. Rhim, P.E. Oberstein, D.H. Thomas, E.T. Mirek, C.F. Palermo, B.Z. Stanger, Article Stromal Elements Act to Restrain, Rather Than Support, Pancreatic Ductal Adenocarcinoma, Cancer Cell 25 (2014) 735–747, https://doi.org/10.1016/j.ccr.2014.04.021.
[13] D.V.T. Catenacci, M.R. Junttila, T. Karrison, N. Bahary, M.N. Horiba, H.L. Kindler, Randomized phase Ib/II study of gemcitabine plus placebo or vismodegib, a hedgehog pathway inhibitor, in patients with metastatic pancreatic cancer, Journal of Clinical Oncology 33 (2015) 4284–4292, https://doi.org/10.1200/JCO.2015.62.8719.
[14] M.V. Apte, P.S. Haber, T.L. Applegate, I.D. Norton, G.W. McCaughan, M.A. Korsten, R.C. Pirola, J.S. Wilson, Periacinar stellate shaped cells in rat pancreas: identification, isolation, and culture, Gut 43 (1998) 128–133, https://doi.org/10.1136/GUT.43.1.128.
[15] M.V. Apte, P.S. Haber, S.J. Darby, S.C. Rodgers, G.W. McCaughan, M.A. Korsten, R. C. Pirola, J.S. Wilson, Pancreatic stellate cells are activated by proinflammatory cytokines: implications for pancreatic fibrogenesis, Gut 44 (1999), https://doi.org/10.1136/gut.44.4.534.
[16] P. Maneshi, J. Mason, M. Dongre, D. Öhlund, Targeting Tumor-Stromal Interactions in Pancreatic Cancer: impact of Collagens and Mechanical Traits, Front. Cell Dev. Biol. 9 (2021) 1–22, https://doi.org/10.3389/fcell.2021.787485.
[17] C.R. Drifka, A.G. Loeffler, C.R. Esquibel, S.M. Weber, K.W. Eliceiri, W.J. Kao, Human pancreatic stellate cells modulate 3D collagen alignment to promote the migration of pancreatic ductal adenocarcinoma cells, Biomed. MicroDevices 18 (2016), https://doi.org/10.1007/s10544-016-0128-1.
[18] D.R. Principe, K.E. Timbers, L.G. Atia, R.M. Koch, A. Rana, TGFβ signaling in the pancreatic tumor microenvironment, Cancers. (Basel) 13 (2021) 1–20, https://doi.org/10.3390/cancers13205086.
[19] W. Shen, G. Tao, Y. Zhang, B. Cai, J. Sun, Z. Tian, TGF β in pancreatic cancer initiation and progression: two sides of the same coin, Cell Biosci. (2017) 1–7, https://doi.org/10.1186/s13578-017-0168-0.
[20] D. Wu, J. Guo, B. Qi, H. Xiao, TGF-β1 induced proliferation, migration, and ECM accumulation through the SNHG11 /miR-34b / LIF pathway in human pancreatic stellate cells, 68 (2021) 1347–1357.
[21] R.-I. Hata, H. Senoo, 1-Ascorbic Acid 2-Phosphate Stimulates Tissuelike Substance by Skin Fibroblasts, J. Cell Physiol. 138 (1989).
[22] B. Piersma, O.Y. Wouters, S. de Rond, M. Boersema, R.A.F. Gjaltema, R.A. Bank, Ascorbic acid promotes a TGFβ1-induced myofibroblast phenotype switch, Physiol. Rep. 5 (2017) 1–10, https://doi.org/10.14814/phy2.13324.
[23] L. Zylinska, M. Lisek, F. Guo, T. Boczek, Vitamin C Modes of Action in Calcium-Involved Signaling in the Brain, Antioxidants 12 (2023) 231, https://doi.org/10.3390/ANTIOX12020231.
[24] J. Oronowicz, J. Reinhard, P.S. Reinach, S. Ludwiczak, H. Luo, M.H. Omar Ba Salem, M.M. Kraemer, H. Biebermann, V. Kakkassery, S. Mergler, Ascorbate-induced oxidative stress mediates TRP channel activation and cytotoxicity in human etoposide-sensitive and -resistant retinoblastoma cells, Laboratory Investig 101 (2021) 70–88, https://doi.org/10.1038/s41374-020-00485-2.
[25] G.G. Martinovich, I.V. Martinovich, S.N. Cherenkevich, Effects of ascorbic acid on calcium signaling in tumor cells, Bull. Exp. Biol. Med. 147 (2009) 469–472, https://doi.org/10.1007/S10517-009-0555-6.
[26] S. Radoslavova, A. Folcher, T. Lefebvre, K. Kondratska, S. Guénin, I. Dhennin-duthille, M. Gautier, N. Prevarskaya, H. Ouadid-ahidouch, Orai1 channel regulates human-activated pancreatic stellate cell proliferation and TGFβ1 secretion through the Akt signaling pathway, Cancers. (Basel) 13 (2021) 1–24, https://doi.org/10.3390/cancers13102395.
[27] V. Szabó, N. Csákány-Papp, M. Görög, T. Madácsy, Á. Varga, J. Maléth, Orai1 calcium channel inhibition prevents progression of chronic pancreatitis, JCI. Insight. 8 (2023), https://doi.org/10.1172/jci.insight.167645.
[28] R.T. Waldron, Y. Chen, H. Pham, A. Go, H.Y. Su, C. Hu, L. Wen, S.Z. Husain, C. A. Sugar, J. Roos, S. Ramos, A. Lugea, M. Dunn, K. Stauderman, S.J. Pandol, The Orai Ca^{2+} channel inhibitor CM4620 targets both parenchymal and immune cells to reduce inflammation in experimental acute pancreatitis, J. Physiol. 597 (2019) 3085–3105, https://doi.org/10.1113/JP277856.
[29] C.P. Leblond, Synthesis and secretion of collagen by cells of connective tissue, bone, and dentin, Anat. Rec. 224 (1989) 123–138, https://doi.org/10.1002/ar.1092240204.
[30] R.M. Feakins, A. Seedhar, G. Elia, I.R. Hart, H.M. Kocher, Organotypic culture model of pancreatic cancer demonstrates that stromal cells modulate E-cadherin, beta-catenin, and Ezrin expression in tumor cells, Am. J. Pathol. 175 (2009) 636–648, https://doi.org/10.2353/ajpath.2009.090131.
[31] L.C.U. Junqueira, G. Bignolas, R.R. Brentani, Picrosirius staining plus polarization microscopy, a specific method for collagen detection in tissue sections, Histochem. J. 11 (1979) 447–455, https://doi.org/10.1007/BF01002772.
[32] C. Szász, D. Pap, B. Szebeni, P. Bokrossy, L. Őrfi, A.J. Szabó, Á. Vannay, A. Veres-Székely, Optimization of Sirius Red-Based Microplate Assay to Investigate Collagen Production In Vitro, Int. J. Mol. Sci. 24 (2023), https://doi.org/10.3390/IJMS242417435.
[33] L.F. Nielsen, D. Moe, S. Kirkeby, C. Garbarsch, Sirius red and acid fuchsin staining mechanisms, Biotechn Histochem 73 (1998) 71–77, https://doi.org/10.3109/10520299809140509.
[34] M.-A. Bray, A. Carpenter, B.I. of M, H. Imaging Platform, Advanced Assay Development Guidelines for Image-Based High Content Screening and Analysis, Assay Guidance Manual (2017). https://www.ncbi.nlm.nih.gov/books/NBK126174/.
[35] J. Franco-Barraza, D.A. Beacham, M.D. Amatangelo, E. Cukierman, Preparation of Extracellular Matrices Produced by Cultured and Primary Fibroblasts, Curr. Protoc. Cell Biol. 71 (2016), https://doi.org/10.1002/CPCB.2, 10.9.1-10.9.34.
[36] R. Kaukonen, G. Jacquemet, H. Hamidi, J. Ivaska, Cell-derived matrices for studying cell proliferation and directional migration in a complex 3D microenvironment, Nat. Protoc. 12 (2017) 2376–2390, https://doi.org/10.1038/nprot.2017.107.
[37] A. Kuntze, O. Goetsch, B. Fels, K. Najder, A. Unger, M. Wilhelmi, S. Sargin, S. Schimmelpfennig, I. Neumann, A. Schwab, Z. Pethő, Protonation of Piezo1 Impairs Cell-Matrix Interactions of Pancreatic Stellate Cells, Front. Physiol. 11 (2020) 89, https://doi.org/10.3389/fphys.2020.00089.
[38] Z. Pethő, K. Najder, S. Beel, B. Fels, I. Neumann, S. Schimmelpfennig, S. Sargin, M. Wolters, K. Grantins, E. Wardelmann, M. Mitkovski, A. Oeckinghaus, A. Schwab, Acid-base homeostasis orchestrated by NHE1 defines pancreatic stellate cell phenotype in pancreatic cancer, JCI. Insight. (2023), https://doi.org/10.1172/JCI.INSIGHT.170928.
[39] T. Loeck, M. Rugi, L.M. Todesca, B. Soret, I. Neumann, S. Schimmelpfennig, K. Najder, Z. Pethő, V. Farfariello, N. Prevarskaya, A. Schwab, The context-dependent role of the Na^{+}/Ca^{2+}-exchanger (NCX) in pancreatic stellate cell migration, Pflugers. Arch. 475 (2023) 1225–1240, https://doi.org/10.1007/s00424-023-02847-3.
[40] L.I. Abd Ali, A.F. Qader, M.I. Salih, H.Y. Aboul-Enein, Sensitive spectrofluorometric method for the determination of ascorbic acid in pharmaceutical nutritional supplements using acriflavine as a fluorescence reagent, Luminescence 34 (2019) 168–174, https://doi.org/10.1002/bio.3589.
[41] V. Gérard, E. Ay, F. Morlet-Savary, B. Graff, C. Galopin, T. Ogren, W. Mutilangi, J. Lalevée, Thermal and Photochemical Stability of Anthocyanins from Black Carrot, Grape Juice, and Purple Sweet Potato in Model Beverages in the Presence of Ascorbic Acid, J. Agric. Food Chem. 67 (2019) 5647–5660, https://doi.org/10.1021/acs.jafc.9b01672.
[42] S. Radoslavova, B. Fels, Z. Pethö, M. Gruner, T. Ruck, S.G. Meuth, A. Folcher, N. Prevarskaya, A. Schwab, H. Ouadid-Ahidouch, TRPC1 channels regulate the activation of pancreatic stellate cells through ERK1/2 and SMAD2 pathways and perpetuate their pressure-mediated activation, Cell Calcium 106 (2022), https://doi.org/10.1016/J.CECA.2022.102621.
[43] B. Fels, N. Nielsen, A. Schwab, Role of TRPC1 channels in pressure-mediated activation of murine pancreatic stellate cells, Eur. Biophys. J. 45 (2016) 657–670, https://doi.org/10.1007/s00249-016-1176-4.
[44] L. Aumailley, S. Bourassa, C. Gotti, A. Droit, M. Lebel, Vitamin C modulates the levels of several proteins of the mitochondrial complex III and its activity in the mouse liver, Redox. Biol. 57 (2022) 102491, https://doi.org/10.1016/j.redox.2022.102491.
[45] X. Zhang, P. Xin, R.E. Yoast, S.M. Emrich, M.T. Johnson, T. Pathak, J.C. Benson, I. Azimi, D.L. Gill, G.R. Monteith, Distinct pharmacological profiles of ORAI1, ORAI2, and ORAI3 channels, Cell Calcium (2020) 1–18, https://doi.org/10.1016/j.ceca.2020.102281.Distinct.
[46] S.J.A. Aper, A.C.C. Van Spreeuwel, M.C. Van Turnhout, A.J. Van Der Linden, P. A. Pieters, N.L.L. Van Der Zon, S.L. De La Rambelje, C.V.C. Bouten, M. Merkx, Colorful protein-based fluorescent probes for collagen imaging, PLoS. One 9 (2014) 1–21, https://doi.org/10.1371/journal.pone.0114983.
[47] K.N. Krahn, C.V.C. Bouten, S. Van Tuijl, M.A.M.J. Van Zandvoort, M. Merkx, Fluorescently labeled collagen binding proteins allow specific visualization of collagen in tissues and live cell culture, Anal. Biochem. 350 (2006) 177–185, https://doi.org/10.1016/j.ab.2006.01.013.
[48] S. SenGupta, C.A. Parent, J.E. Bear, The principles of directed cell migration, Nat. Rev. Mol. Cell Biol. 22 (2021) 529–547, https://doi.org/10.1038/s41580-021-00366-6.
[49] O. Olajubutu, O.D. Ogundipe, A. Adebayo, S.K. Adesina, Drug Delivery Strategies for the Treatment of Pancreatic Cancer, Pharmaceutics. (2023) 15, https://doi.org/10.3390/pharmaceutics15051318.
[50] I. Bogeski, C. Kummerow, D. Al-Ansary, E.C. Schwarz, R. Koehler, D. Kozai, N. Takahashi, C. Peinelt, D. Griesemer, M. Bozem, Y. Mori, M. Hoth, B. A. Niemeyer, Differential redox regulation of ORAI ion channels: a mechanism to tune cellular calcium signaling, Sci. Signal. 3 (2010), https://doi.org/10.1126/SCISIGNAL.2000672.
[51] A. Maul-Pavicic, S.C.C. Chiang, A. Rensing-Ehl, B. Jessen, C. Fauriat, S.M. Wood, S. Sjöqvist, M. Hufnagel, I. Schulze, T. Bass, W.W. Schamel, S. Fuchs, H. Pircher, C. A. McCarl, K. Mikoshiba, K. Schwarz, S. Feske, Y.T. Bryceson, S. Ehl, ORAI1-mediated calcium influx is required for human cytotoxic lymphocyte degranulation and target cell lysis, Proc. Natl. Acad. Sci. u S. a 108 (2011) 3324–3329, https://doi.org/10.1073/pnas.1013285108.
[52] H. Balghi, R. Robert, B. Rappaz, X. Zhang, A. Wohlhuter-Haddad, J.W. Hanrahan, Enhanced Ca2+ entry due to Orai1 plasma membrane insertion increases IL-8 secretion by cystic fibrosis airways, FASEB J. 25 (2011) 4274–4291, https://doi.org/10.1096/fj.11-187682.
[53] J.C. Hay, Calcium: a fundamental regulator of intracellular membrane fusion? EMBo Rep. 8 (2007) 236–240, https://doi.org/10.1038/sj.embor.7400921.
[54] W.A. Cabral, M. Ishikawa, M. Garten, E.N. Makareeva, B.M. Sargent, M.A. Weis, J. C. Marini, Absence of the ER cation channel TMEM38B/TRIC-B disrupts intracellular calcium homeostasis and dysregulates collagen synthesis in recessive osteogenesis imperfecta, PLoS. Genet. 12 (2016) 1–27, https://doi.org/10.1371/journal.pgen.1006156.
[55] A.B. Parekh, Store-operated CRAC channels: function in health and disease, Nat. Rev. Drug Discov. 9 (2010) 399–410, https://doi.org/10.1038/nrd3136.
[56] X. Zhang, P. Xin, R.E. Yoast, S.M. Emrich, M.T. Johnson, T. Pathak, J.C. Benson, I. Azimi, D.L. Gill, G.R. Monteith, M. Trebak, Distinct pharmacological profiles of

ORAI1, ORAI2, and ORAI3 channels, Cell Calcium 91 (2020), https://doi.org/10.1016/J.CECA.2020.102281.
[57] M.G. Espey, P. Chen, B. Chalmers, J. Drisko, A.Y. Sun, M. Levine, Q. Chen, Pharmacologic ascorbate synergizes with gemcitabine in preclinical models of pancreatic cancer, Free Radic. Biol. Med. 50 (2012) 1610–1619, https://doi.org/10.1016/j.freeradbiomed.2011.03.007.
[58] J. Cieslak, J. Cullen, Treatment of Pancreatic Cancer with Pharmacological Ascorbate, Curr. Pharm. Biotechnol. 16 (2015) 759–770, https://doi.org/10.2174/1389201016091507151359 21.
[59] Q. Chen, M.G. Espey, M.C. Krishna, J.B. Mitchell, C.P. Corpe, G.R. Buettner, E. Shaded, M. Levine, Pharamacologic ascorbic acid concentrations selectively kill cancer cells: action as a pro-drug to deliver hydrogen peroxide to tissuses, Proc. Natl. Acad. Sci. u S. a 102 (2005) 13604–13609, https://doi.org/10.1073/pnas.0506390102.
[60] J. Du, S.M. Martin, M. Levine, B.A. Wagner, G.R. Buettner, S.H. Wang, A. F. Taghiyev, C. Du, C.M. Knudson, J.J. Cullen, Mechanisms of ascorbate-induced cytotoxicity in pancreatic cancer, Clin. Cancer Res. 16 (2010) 509–520, https://doi.org/10.1158/1078-0432.CCR-09-1713.
[61] K.A. Stauderman, CRAC channels as targets for drug discovery and development, Cell Calcium 74 (2018) 147–159, https://doi.org/10.1016/j.ceca.2018.07.005.
[62] C. Bruen, M. Al-Saadi, E.A. Michelson, M. Tanios, R. Mendoza-Ayala, J. Miller, J. Zhang, K. Stauderman, S. Hebbar, P.C. Hou, Auxora vs. placebo for the treatment of patients with severe COVID-19 pneumonia: a randomized-controlled clinical trial, Crit. Care 26 (2022), https://doi.org/10.1186/S13054-022-03964-8.
[63] S.R. Hingorani, L. Wang, A.S. Multani, C. Combs, T.B. Deramaudt, R.H. Hruban, A. K. Rustgi, S. Chang, D.A. Tuveson, Trp53R172H and KrasG12D cooperate to promote chromosomal instability and widely metastatic pancreatic ductal adenocarcinoma in mice, Cancer Cell 7 (2005) 469–483, https://doi.org/10.1016/j.ccr.2005.04.023.
[64] S.R. Hingorani, E.F. Petricoin, A. Maitra, V. Rajapakse, C. King, M.A. Jacobetz, D. A. Tuveson, Preinvasive and invasive ductal pancreatic cancer and its early detection in the mouse, Cancer Cell 4 (2003) 437–450, https://doi.org/10.1016/S1535-6108(03)00309-X.
[65] M. Gannon, P.-L. Herrera, C.V.E. Wright, Mosaic Cre-Mediated Recombination in Pancreas Using the pdx-1 Enhancer/Promoter, (2000). https://doi.org/10.1002/(SICI)1526-968X(200002)26:2.
[66] S. Fuest, C. Post, S.T. Balbach, S. Jabar, I. Neumann, S. Schimmelpfennig, S. Sargin, E. Nass, T. Budde, S. Kailayangiri, B. Altvater, A. Ranft, W. Hartmann, U. Dirksen, C. Rössig, A. Schwab, Z. Pethő, Relevance of Abnormal KCNN1 Expression and Osmotic Hypersensitivity in Ewing Sarcoma, Cancers. (Basel) (2022) 4819, https://doi.org/10.3390/CANCERS14194819, 2022, Vol. 14, Page 4819 14.
[67] T. Chepda, M. Cadau, P. Girin, J. Frey, A. Chamson, Monitoring of ascorbate at a constant rate in cell culture: effect on cell growth, In. Vitro Cell Dev. Biol. Anim. 37 (2001) 26–30, https://doi.org/10.1290/1071-2690(2001)037<0026:MOAAAC>2.0.CO;2.
[68] J. Franco-barraza, K.S. Raghavan, T. Luong, E. Cukierman, T. Martin, F. Chase, Engineering clinically-relevant human fibroblastic cell-derived extracellular matrices, (2021). https://doi.org/10.1016/bs.mcb.2019.11.014. Engineering.
[69] P. Bankhead, M.B. Loughrey, J.A. Fernández, Y. Dombrowski, D.G. McArt, P. D. Dunne, S. McQuaid, R.T. Gray, L.J. Murray, H.G. Coleman, J.A. James, M. Salto-Tellez, P.W. Hamilton, QuPath: open source software for digital pathology image analysis, Sci. Rep. 7 (2017) 16878, https://doi.org/10.1038/s41598-017-17204-5.
[70] B. Vogel, H. Siebert, U. Hofmann, S. Frantz, Determination of collagen content within picrosirius red stained paraffin-embedded tissue sections using fluorescence microscopy, MethodsX. 2 (2015) 124–134, https://doi.org/10.1016/j.mex.2015.02.007.
[71] A. Feher, Z. Pethő, T.G. Szanto, Á. Klekner, G. Tajti, G. Batta, T. Hortobágyi, Z. Varga, A. Schwab, G. Panyi, Mapping the functional expression of auxiliary subunits of $K_{Ca}1.1$ in glioblastoma, Sci. Rep. 12 (2022), https://doi.org/10.1038/S41598-022-26196-W.
[72] N. Nielsen, K. Kondratska, T. Ruck, B. Hild, I. Kovalenko, S. Schimmelpfennig, J. Welzig, S. Sargin, O. Lindemann, S. Christian, S.G. Meuth, N. Prevarskaya, A. Schwab, TRPC6 channels modulate the response of pancreatic stellate cells to hypoxia, Pflugers. Arch. 469 (2017) 1567–1577, https://doi.org/10.1007/S00424-017-2057-0.
[73] J.E. Merritt, R. Jacob, T.J. Hallam, Use of Manganese to Discriminate between Calcium Influx and Mobilization from Internal Stores in Stimulated Human Neutrophils, J. Biol. Chem. 264 (1989) 1522–1527, https://doi.org/10.1016/S0021-9258(18)94218-3.